

NEW ICOSAHEDRAL BORON CARBIDE SEMICONDUCTORS

by

Elena Maria Echeverria Mora

A DISSERTATION

Presented to the Faculty of

The Graduate College at the University of Nebraska

In Partial Fulfilment of Requirements

For the Degree of Doctor of Philosophy

Major: Physics and Astronomy

Under the Supervision of Peter A. Dowben

Lincoln, Nebraska

July, 2017

NEW ICOSAHEDRAL BORON CARBIDE SEMICONDUCTORS

Elena Maria Echeverria Mora, Ph.D.

University of Nebraska, 2017

Adviser: Peter A. Dowben

Novel semiconductor boron carbide films and boron carbide films doped with aromatic compounds have been investigated and characterized. Most of these semiconductors were formed by plasma enhanced chemical vapor deposition. The aromatic compound additives used, in this thesis, were pyridine (Py), aniline, and diaminobenzene (DAB).

As one of the key parameters for semiconducting device functionality is the metal contact and, therefore, the chemical interactions or band bending that may occur at the metal/semiconductor interface, X-ray photoemission spectroscopy has been used to investigate the interaction of gold (Au) with these novel boron carbide-based semiconductors. Both n- and p-type films have been tested and pure boron carbide devices are compared to those containing aromatic compounds. The results show that boron carbide seems to behave differently from other semiconductors, opening a way for new analysis and approaches in device's functionality.

By studying the electrical and optical properties of these films, it has been found that samples containing the aromatic compound exhibit an improvement in the electron-hole separation and charge extraction, as well as a decrease in the band gap. The hole carrier lifetimes for each sample were extracted from the capacitance-voltage, C(V), and current-voltage, I(V), curves. Additionally, devices, with boron carbide with the addition of pyridine, exhibited better collection of neutron capture generated pulses at ZERO applied bias,

compared to the pure boron carbide samples. This is consistent with the longer carrier lifetimes estimated for these films.

The I-V curves, as a function of external magnetic field, of the pure boron carbide films and films containing DAB demonstrate that significant room temperature negative magneto-resistance (> 100% for pure samples, and >50% for samples containing DAB) is possible in the resulting dielectric thin films. Inclusion of DAB is not essential for significant negative magneto-resistance, however, these results suggest practical device applications, especially as such effects are manifested in nanoscale films with facile fabrication. Overall, the greater negative magneto-resistance, when undoped with an aromatic, suggests a material with more defects and is consistent with a shorter carrier lifetime.

Table of Contents

Table of Contents	iv
List of Figures	vii
List of Tables	x
1 INTRODUCTION	1
References	4
2 EXPERIMENTAL TECHNIQUES	8
2.1 Introduction	8
2.2 Fabrication Techniques	9
2.2.1 Electron Beam Induced Cross-linking (EBIC)[1-3,5,6]	9
2.2.2 Plasma-Enhanced Chemical Vapor Deposition (PECVD) [3,7-9] . .	12
2.3 X-ray Photoelectron Spectroscopy (XPS)	13
2.4 Variable angle spectroscopic ellipsometry (VASE)	17
2.4.0.1 Band Gap Determination	20
2.5 Electrical and Transport Measurements	21
References	23

3 GOLD (Au) CONTACTS	26
3.1 Introduction	26
3.2 Metal-Semiconductor Contacts: Theory	27
3.2.1 Schottky Barrier Diodes	29
3.2.2 Ohmic Contacts	31
3.3 Au/Boron Carbide Based Semiconductors	32
3.3.1 <i>ortho</i> -carborane based Samples	34
3.3.1.1 Before Au Deposition	34
3.3.1.2 After Au Deposition	39
3.3.1.3 After Ar ⁺ Sputtering	46
3.3.2 <i>meta</i> -carborane based Samples	47
References	53
4 PYRIDINE	57
4.1 Introduction	57
4.2 Samples Composition	57
4.3 Spectroscopic ellipsometry	59
4.4 Device Heterostructures	62
4.5 Neutron Capture	66
References	70
5 MAGNETO-RESISTANCE	75
5.1 Introduction	75
5.2 Photoemission Spectroscopy	76
5.3 Magnetoresistance Measurements	78
5.3.1 Basic Principles	78

5.3.2 Negative Magnetoresistance	79
References	84
6 CONCLUSIONS	87
7 FUTURE DIRECTIONS	89

List of Figures

1.1	^{14}N neutron capture in a PECVD polymerized pyridine film. The Q-value of this reaction is 626 keV. Taken from [22]	2
2.1	Graphical model of two of the three carborane isomers.	10
2.2	Chemical Structure of the aromatics compounds used in this study.	10
2.3	The schematic structural models of the $B_{10}C_2H_{12}$ (left), and $B_{10}C_2H_{12}:Y$ (right). .	11
2.4	Schematic picture of the PECVD chamber. Modified from [7].	12
2.5	Schematic picture describing the photoelectron emission (right), and energy reference levels (left).	15
2.6	Schematic picture describing the Auger electron emission.	16
2.7	XPS configuration.	17
2.8	Basic procedure to determine some properties of a material being studied using VASE [16].	19
2.9	Equipment for magnetoresistance measurements	22
3.1	Energy band diagram for a) metal a b) n-type semiconductor. Taken from [4]. .	28
3.2	Energy band diagram for a Schottky barrier. Taken from [4].	29
3.3	Energy band diagram for p-type semiconductor when $\Phi_M < \Phi_S$	30
3.4	Energy band diagram for n-type semiconductor when $\Phi_M < \Phi_S$	31
3.5	Energy band diagram for p-type semiconductor when $\Phi_M > \Phi_S$	32

3.6	Deconvoluted XPS spectra of the B(1s), C(1s) and O(1S) core levels.	36
3.7	Deconvoluted XPS spectra of the B(1s), C(1s), O(1s) and N(1s) core levels. . .	38
3.8	XPS core level spectra of the B(1s) (Top), and C(1s) (bottom) as a function of the Au deposition.	39
3.9	Evolution of the deconvoluted core level spectra of the B(1s) (left), and C(1s) (right) as a function of the Au deposition.	42
3.10	Deconvoluted XPS spectra of the B(1s), C(1s), and O(1s) core levels for the pure boron carbide (<i>o</i> -BC) film.	43
3.11	XPS core level spectra of the B(1s) (Top), and C(1s) (bottom) as a function of the Au deposition.	44
3.12	Evolution of the deconvoluted core level spectra of the B(1s) (left), C(1s) (middle) and N(1s) (right) as a function of the Au deposition.	45
3.13	XPS core level spectra of the B (1s) when the sample was cleaned (top), after last Au deposition (middle), and after last Ar ⁺ sputtering (bottom).	46
3.14	Evolution of the deconvoluted core level spectra of the B(1s) (left), and C(1s) (right) as a function of the Au deposition.	48
3.15	Shift in the binding energy of the B(1s) peak with increasing Au overlayer thickness.	50
3.16	XPS core level spectra of the B(1s) (Top), and C(1s) (bottom) as a function of the Au deposition.	51
4.1	Dielectric function spectra for <i>o</i> -BC (dotted line) and <i>o</i> -BCPy(1:3) (solid line) films.	59
4.2	Band gap energy as a function of pyridine inclusion.	61
4.3	Comparison of the UPS spectra of the valence bands.	61
4.4	I(V) curves for pure samples and samples with pyridine.	62

4.5	Reverse bias current normalized to the 3 V forward bias current.	63
4.6	C(V) curves for the heterojunctions as a function of the frequency.	63
4.7	Model of diffusion capacitance overlaid on C(V) data at 10 kHz.	65
4.8	The experimental neutron pulse height spectra at ZERO applied bias.	68
5.1	Core level spectrum of the B(1s), C(1s), O(1s) and N(1s) core levels for cross-linking <i>ortho</i> -carborane with DAB additions (BC:DAB) films.	76
5.2	Comparison of the UPS spectra.	78
5.3	Schematic picture of the configuration to get giant magnetoresistance.	79
5.4	Magnetoresistance for a BC:DAB film at room temperature.	80
5.5	I(V) Curves with an external applied magnetic field	81
7.1	Schematic of the Makrolon TM plate assembly.	90
7.2	I(V) curve for boron carbide with pyridine before (black line), after 28 hours (red line), and after 84 hours (blue line) of neutron irradiation.	90

List of Tables

3.1	Chemical Composition.	35
3.2	XPS measured binding energies for B(1s), C(1s), and N(1s) core levels.	35
3.3	Relative atomic concentrations obtained by XPS for gold, boron, carbon, oxygen and nitrogen.	41
3.4	Binding energy shift for all elements present in each sample.	43
3.5	XPS measured binding energies for the B(1s), C(1s), and N(1s) core levels: before and after Au deposition and after cleaning.	47
3.6	XPS measured binding energies for the B(1s), and C(1s) core levels components. .	49
4.1	Experimental B/N and B/C atomic ratios, and corresponding pyridine/orthocarbon ratios.	58
4.2	Calculated thickness and band gaps of the studied films.	60
4.3	Hole carrier lifetimes of the studied films.	66

Chapter 1

INTRODUCTION

Semiconducting boron carbides have been well known for their applications as semiconductors suitable for solid state neutron detectors [1-4], as well as their potential for spintronics and semiconductor devices in harsh environments [5-7]. Their applications are limited mainly by the high defect concentrations and low carrier mobilities [8,9] of the typical semiconducting boron carbides, but they are found to be very robust with respect the radiation damage, i.e. they are self healing with modest amounts of radiation damage.

What is key to the general motivation behind this work is that modifications to boron carbide may result in a better boron carbide that might overcome the natural limitations of the more conventional boron carbides. If these devices can capture neutrons at zero applied bias, then neutron voltaics are possible, as well as low power neutron detectors. This is important, because, these semiconductors are commonly used as neutron detectors for identifying nuclear materials used in weapons, or even to detect and treat cancer [10,11].

It is also known that not only defects in boron carbide based semiconductors materials can play an important role in the functionality of the device [12-15], but also the carbon to boron ratio [16,17,20,21]. Previous studies have shown that the boron carbide band gap

decreases with increasing the carbon concentration, its values varies from 0.77 eV (highest carbon concentration) to 1.8 eV [20-21], affecting the conductivity of the sample and therefore the electric transport measurements in the boron carbide based samples [18].

Novel boron carbide semiconductors, with aromatic moiety inclusions are seen [19] to be good candidate materials to study neutron capture, as their properties, like the band gap, can be modified by varying the carbon concentration. On other hand, the presence of nitrogen in the aromatic compounds may marginally increase neutron capture cross-sections at very high neutron energies (584 keV), as seen in Fig. 1.1, where the strong boron capture cross-section falls sharply, without leading to an increase in cross-section to hard X-ray or gamma radiation, since nitrogen and boron are both low Z elements. Therefore, it seems natural to use aromatic compounds as dopings for these heterojunctions.

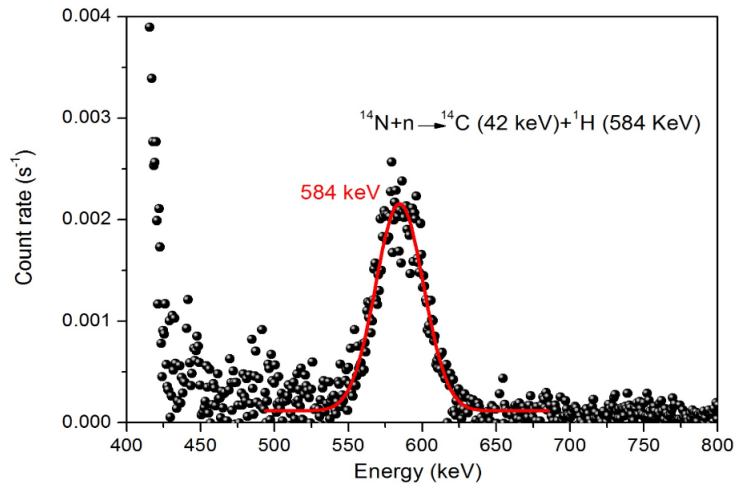


Figure 1.1: ^{14}N neutron capture in a PECVD polymerized pyridine film. The Q-value of this reaction is 626 keV. Taken from [22]

Additionally, semiconducting boron carbides have been shown to be either p-type, in the absence of transition metal doping [23-26], or n-type [27-29]. In the case of a p-type boron

carbide, the lifetimes are of about $30 \mu s$, while these for n-type are $50 ns$. Since these values are several orders of magnitude different, it seems interesting to study both types of conductivities.

Contacts are also an issue. In particular, Au/semiconductor interfaces will be studied to aid in the characterization of these novel semiconducting boron carbides.

In the study of any new semiconductor, a combination of surface science studies and transport studies can prove to be quite effective in developing a better understanding of the potential devices. Thus, chapter 2 will be devoted to describe these techniques, and how samples were growth. Next, in chapter 3 X-ray photoemission spectroscopy will be used to study and characterize the meta/semiconductor interface. Then, chapter 4 will describe the effects of doping films with pyridine by studying the optical properties, the electrical responses, and the neutron capture of heterojunctions containing pyridine, and comparing these results to the pure boron carbide diodes, and the results from doping with benzene and aniline. Finally, magneto-resistance effects, by electrical measurements, will be discussed in chapter 5.

References

- [1] A.N. Caruso. Journal of Physics: Condensed Matter. **22**, 443201 (2010)
- [2] Caruso, A.N., Dowben, P.A., Blakir, S., Schemm, N., Osberg, K., Fairchild, R.W., Flores, O.B., Balaz, S., Harken, A.D., Robertson, B.W., Brand, J.I. Mat. Sci. Eng. B **135** (2006) 129
- [3] Day, E., Diaz, M.J., Adenwalla, S. J. Phys. D: Appl. Phys. **39** (2006) 2920
- [4] Caruso, A.N., Billa, R.B., Balaz, S., Brand, J.I., Dowben, P.A., J. Phys.: Condens. Matter **16** (2004) L139
- [5] Luo, G., Lu, J., Liu, J., Mein, W., Dowben, P.A. Mater. Sci. Eng. B **175** (2010) 1
- [6] Bernard, L., Monson, J., Sokolov, A., Liu, Z.Y, Yang, C.S., Dowben, P.A., Doudin, B., Harken, A., Welsch, P. and Robertson, B.W. Appl. Phys. Lett. **83** (2003) 3743
- [7] Liu, J., Dowben, P.A., Luo, G., Mei, W.-N., Kumar Rajapitamahuni, A., Sokolov, A., Karki, S. and Caruso, A.N. MRS Symposium Proceedings **1307** (2011) DOI:10.1557/opl.2011.503
- [8] M.M. Abdul-Gader, et al. Int. J. Electron, **88** 873 (2001)
- [9] B.J. Nordell et al. Mater. Chem. Phys. **173** 268-284 (2016)

- [10] F.M. Wagner, B. Loeper-Kabasakal and H. Breitkreutz, “Neutron medical treatment of tumours - a survey of facilities”. JINST **7** (2012) C03041
- [11] Oak Ridge National Laboratory. “Neutron detector will advance human disease research” ScienceDaily. ScienceDaily, 6 September 2012
- [12] Caretti, I., and Jiménez, I. Point defects in hexagonal BN, BC₃ and BC_xN compounds studied by x-ray absorption near-edge structure. Journal of /Applied Physics. **110** (2011) 023511
- [13] Cennignani, W., and Pantano, C.G. X-ray Photoelectron Spectroscopy of Boron-Doped carbon.
- [14] Pasquale, F.L., Li, Y., Du, J., and Kelber, J.A. Novel alloy polymers formed from *ortho*-carborane and benzene or pyridine. J. Phys.: Condens. Matter **25** (2013) 105801
- [15] Pasquale, F.L., Liu, J., Dowben, P.A., Kelber, J.A. Novel semiconducting alloy polymers formed from *ortho*-carborane and 1,4-diaminobenzene. Materials Chemistry and Physics **133** (2012) 901-906
- [16] Park, K., Pederson, M.R., Boyer, L.L., Mei, W.N., Sabirianov, R.F., Zeng, X.C., Bulusu, S., Curran, S., Dewald, J., Day, E., Adenwalla, S., Diaz, M., Rosa, L.G., Balaz, S., and Dowben, P.A. Electronic structure and vibrational spectra of C₂B₁₀-based clusters and films. Phys. Rev. B **73** (2006) 035109
- [17] Werheit, H., Rotter, H.W., Meyer, F.D., Hillebrecht, H., Shalamberidze, S.O., Abzianidze, T.G., Esadze, G.G. FT-Raman spectra of isotope-enriched boron carbide. Journal of Solid State Chemistry **177** (2004) 569-574
- [18] Tallant, D.R., Aselage, T.L., Campbell, A.N., and Emin, D. Boron Carbide Structure by Raman Spectroscopy. Physical Review B **40(8)** (1989) 5649

- [19] Pasquale, F.L., James, R., Welch, R., Echeverria, E., Dowben, P.A., and Kelber, J.A. Novel Cross-Linked Ortho-Carborane and Ortho-Carborane:Y (Y=1,4-diaminobenzene, pyridine, benzene) Polymer Films: A New Class of Carborane-Based Materials with Tunable Electronic Structure. *ECS Transactions* **53(1)** (2013) 303-310
- [20] Lee, S., Mazurowski, J., Ramseyer, G., Dowben, P.A. *J. Appl. Phys.* **72(10)** (1992) 4925
- [21] Shirai., K., Emura, S., Gonda, S.I., and Kumashiro, Y. Infrared study of amorphous $B_{1-x}C_x$ films. *J. Appl. Phys.* **78(5)** (1995) 1
- [22] Tan, C., James, R., Dong, B., Driver, M.S., Kelber, J.A., Downing, G., Cao, L.R. Characterization of a boron carbide-based polymer neutron sensor. *Nuclear Instruments and Methods in Physics Research A* **803** (2015) 82-88
- [23] Hwang, S., Yang, K., Dowben P.A., Ahmad, A.A., Ianno, N.J., Li, J.Z., Lin, J.Y., Jiang, H.X., McIlroy, D.N. Fabrication of n-type nickel doped $B_5C_{1+\delta}$ homojunction and heterojunction diodes. *Appl. Phys. Lett.* **70** (1997) 1028
- [24] Hwang, S., Remmes, N.B., Dowben, P.A., McIlroy, D.N. Nickel doping of boron carbide grown by plasma enhanced chemical vapor deposition. *J. Vac. Sci. Technol., B* **14** (1996) 2957
- [25] Hwang, S., Remmes, N., Dowben, P.A., McIlroy, D.N. Nickel doping of boron carbide and corresponding Fermi level shifts. *J. Vac. Sci. Technol. B* **15** (1997) 854
- [26] Carlson, L., Lagraffe, D., Balaz, S., Ignatove, A., Losovyj, Y.B., Choi, J., Dowben, P.A., Brand, J.I. Doping of boron carbides with cobalt, using cobaltocene. *Appl. Phys. A Mater. Sci. Process.* **89** (2007) 195

- [27] Peterson, G., Su, Q., Wang, Y., Dowben, P., Nastasi, M. Improved p-n heterojunction device performance induced by irradiation in amorphous boron carbide films. Mater. Sci. Eng. B 202 (2015) 25
- [28] B.W. Robertson, S. Adenwalla, A. Harken, P. Welsch, J.I. Brand, P.A. Dowben, J.P. Claassen, A class of boron-rich solid-state neutron detectors, Appl. Phys. Lett. 80 (2002) 3644.
- [29] Caruso, A.N., Balaz, S., Xu, B., Dowben, P.A., McMullen-Gunn, A.S., Brand, J.I., Losovyj, Y.B., McIlroy, D.N. Surface photovoltage effects on the isomeric semiconductors of boron-carbide. Appl. Phys. Lett. 84 (2004) 1302

Chapter 2

EXPERIMENTAL TECHNIQUES

Introduction

Experimental techniques are fundamental to the characterization of any material. Knowing how samples are grown or how measurements are going to be carried out allow us to determine the best characterization procedure to follow, or how the samples can be modified in order to improve the quality of the characterization. Since one of our interests is to characterize novel boron carbide materials, this chapter will describe not only the techniques used to fabricate all the boron carbide and boron carbide with the aromatic compound films used in this study, but also all the methods used to characterize these samples.

In this chapter, the focus will be first given to the fabrication processes, then X-ray photoemission experiments will be described, and then information about optical and electrical measurements will be presented.

Fabrication Techniques

Currently, there exist a number of different techniques for fabricating high-quality semiconductor films. Choosing one or the other will depend on the combined source materials available and the semiconductor's applications. For boron carbides with aromatic compounds there exist mainly two known fabrication techniques: Electron beam induced cross-linking (EBIC) and plasma enhanced chemical vapor deposition (PECVD) [1-3]. Each technique will give us not only different thin film thickness range, but also different boron carbide:aromatic compound ratios, being thickness and boron concentration two key parameters in the semiconductor's performance.

The emphasis on chemical vapor deposition techniques rather than single crystal growth techniques is the result of long and unsuccessful history of trying to make a high quality highly resistive boron carbide by single crystal growth techniques. This is beyond the scope of this thesis, but basically CVD techniques work and single crystal growth techniques do not.

Samples¹ are either *ortho*- (see Fig. 2.1a) or *meta*-carborane source compound based films (see Fig. 2.1b). The aromatic compounds used as additives in this study are pyridine (Py), benzene (BZN), diaminobenzene (DAB) and aniline (see Fig. 2.2). Silicon (Si) substrates with a resistivity of $100 \Omega\cdot\text{cm}$ were used as a substrate for all films.

Electron Beam Induced Cross-linking (EBIC)[1-3,5,6]

Electron beam processing is a procedure where the semiconductor material was fabricated through irradiation of condensed films of molecules, with an electron beam, to initiate

¹ Samples were fabricated by collaborators (Dr. Jeffry A. Kelber's Group) at University of North Texas.

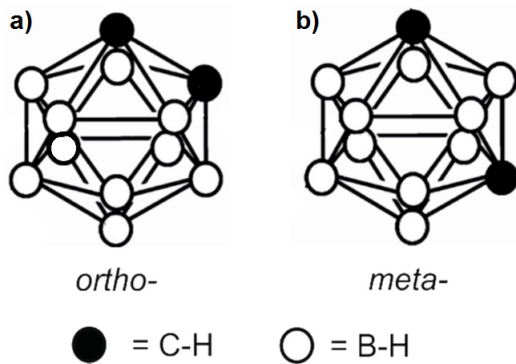


Figure 2.1: Graphical model of two of the three carborane isomers (*clos*o- $C_2B_{10}H_{12}$) a) *ortho*- and b) *meta*-carborane [4]. The hydrogen is left off for clarity.

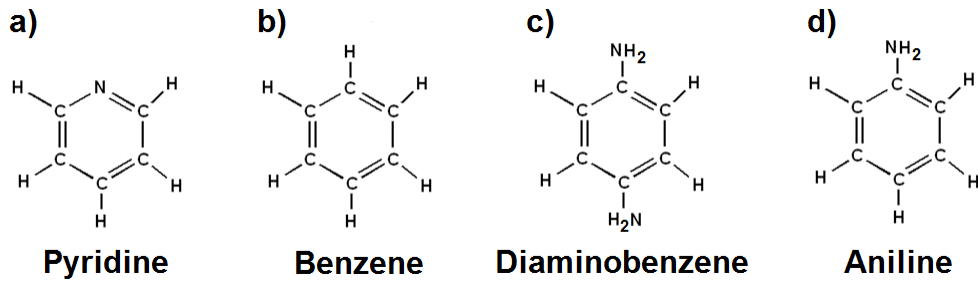


Figure 2.2: Chemical Structure of the aromatics compounds used in this study. a) pyridine, b) benzene, c) diaminobenzene and d) aniline.

intermolecular cross linking. Cycles of condensation, then followed by electron-induced cross-linking, were repeated in order to get a thin film ($\sim 100 \text{ \AA}$) of a hydrogenated boron carbide. After these cycles are completed, samples were allowed to warm back to room temperature, and then annealed to 600 K to assure that any impurity or non-crosslinked compounds are removed from the sample. For these studies, all processes were performed under ultra high vacuum conditions (low 10^{-10} Torr).

A leak valve was used to control the (*ortho/meta*)-carborane partial pressure. A different manual leak valve is used to admit and control the concentration of the linking group (benzene, diaminobenzene, pyridine or aniline) into the UHV chamber during the deposition process. The condensation process was carried out by exposing the material to about 10

Langmuir ($L = 10^{-6}$ Torr·s) on clean Si (100) substrate, cooled with liquid nitrogen cryostat.

Here in this work, condensed (*ortho/meta*)-carborane films were bombarded with a 200 eV electron beam at low temperatures (~ 110 K). As a result, cross-linking of the icosahedral units seem to be preserved. Fig. 2.3 shows the proposed molecular structure for *ortho*-carborane linked with the aromatic compounds.

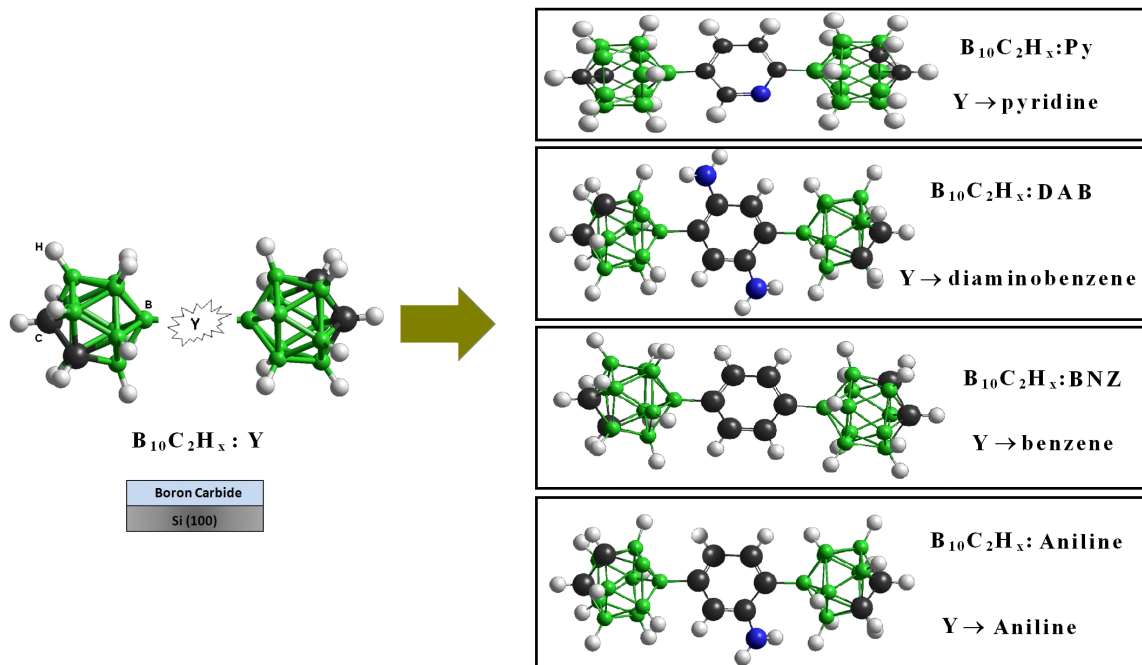


Figure 2.3: The schematic structural models of the $B_{10}C_2H_{12}$ (left), and $B_{10}C_2H_{12}:Y$ (right), with Y representing the aromatic compound (pyridine, diaminobenzene, benzene and aniline) [1].

The (*ortho/meta*)-carborane and linking groups were obtained from commercial sources. The electron gun emission current and beam energy values were kept same for each deposition in order to ensure constant electron flux, and therefore, same settings for different aromatic compounds (also called linking groups) [5]. This may not ensure uniform cross-linking because cross-sections may differ for the different aromatic compounds.

Plasma-Enhanced Chemical Vapor Deposition (PECVD) [3,7-9]

Plasma-enhanced chemical vapor deposition (PECVD) was carried out in a custom-built chamber (see Fig. 2.4) under high vacuum conditions (low 10^{-7} Torr) by the Kelber group (University of North Texas), however, pressure reaches a maximum of \sim 50-70 mTorr during the deposition process to ensure plasma production. The (*ortho/meta*)-carborane precursors were deposited on clean Si(100). While in EBIC process, the silicon substrate was held at low temperatures, here with PECVD, the substrate was kept at or near room temperature. Inductively-coupled Ar⁺ plasma (ICP) was generated by a modified 2.75 CF-metal glass seal using a 13.56 MHz RF generator.

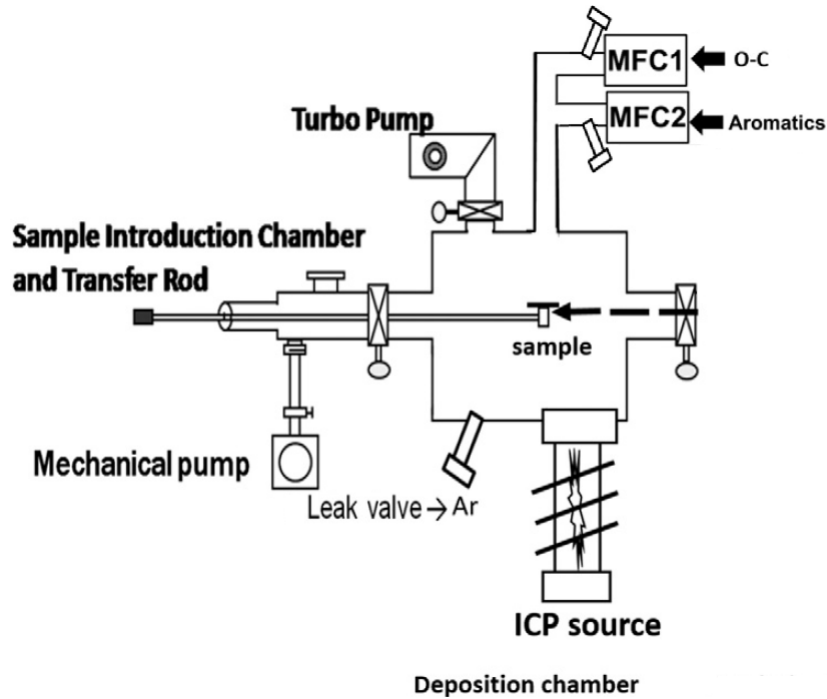


Figure 2.4: Schematic picture of the PECVD chamber. Modified from [7].

Precursors and aromatic compounds, from commercial sources, were purified by freeze-pump-thaw procedures, as developed in Nebraska, and introduced into the deposition cham-

ber using mass flow controllers (MFC). The sublimation of the precursors and aromatic compounds was carried out by heating their containers with heating tapes, which allows an uniform heating process. Once the desired source molecule vapor pressure was reached, the vapor is introduced into the deposition chamber. The needed temperature to evaporate or sublimate the source precursors is ~ 330 K, while for the aromatic compounds was ~ 350 K.

Composite films with different carborane to aromatic ratios were formed by varying the flow rate of the linking group into the PECVD chamber, with a constant flow rate of (*ortho/meta*)-carborane at 5 sccm (standard cubic centimeter per minute). For films with aromatic/(*ortho/meta*)-carborane ratios of $\sim 2:1$, $\sim 3:1$, $\sim 5:1$ $\sim 7:1$, and $\sim 10:1$, aromatic flow rates of 5 sccm, 7 sccm, 20 sccm, 30 sccm, and 35 sccm, were used respectively. This procedure provides a high degree of reproducibility of films composition.

The benefit of using PECVD compared to EBIC is the feasibility of growing thicker samples, from several nm to > 1000 nm. Additionally, the PECVD leads to more dehydrogenation, reducing the hydrogen content contained within the film during the growth process, therefore forming a nonvolatile semiconductor, and have shown to be boron-rich compared to those growth by EBIC.

X-ray Photoelectron Spectroscopy (XPS)

X-ray Photoelectron Spectroscopy (XPS), also known as X-ray photoemission spectroscopy, is one of the most common surfaces characterization methods. This is a technique that not only gives useful information about the composition of the samples, but also, it helps to identify the type of bonding configurations present in the material. In identifying the com-

position of the sample, binding energies are calculated and compared to these reported in the literature.

XPS works by using the principles of the photoelectric effect. Electrons from the core level are sent out from the target by photons created by the X-ray source (Fig. 2.5). These electrons are detected by an electron analyzer, and then their kinetic energy is measured. This process can be seen as a three-step process [10]:

1. The photon generated by the X-ray source is absorbed by an atom, exciting an electron from a core level. The electron absorb enough energy to move from a initial state (E_i) to an final or excited state (E_n).
2. The photo-electron travels to the surface of the sample.
3. If the electron has ratains enough energy, it can overcome the work function of the system (ϕ_{sys}), and be ejected into the vacuum with a kinetic energy (KE), and then it can be detected by the electron analyzer.

Therefore, by energy conservation, the energy provided by the X-ray photon can be written as:

$$h\nu = KE + E_B + \phi_{sys} \quad (2.1)$$

where $E_B = E_n - E_i$ is the binding energy of the electron. For semiconductors, it is typical to reference the final state of the electron to either the valence band maximum or the Fermi level (E_F). Then, in the case of the Fermi level, $E_B = E_F - E_i$ [11,12], as seen in Fig. 2.5. Consequently, by knowing the kinetic energy (KE) of the detected electron, it is possible to know the initial state binding energy.

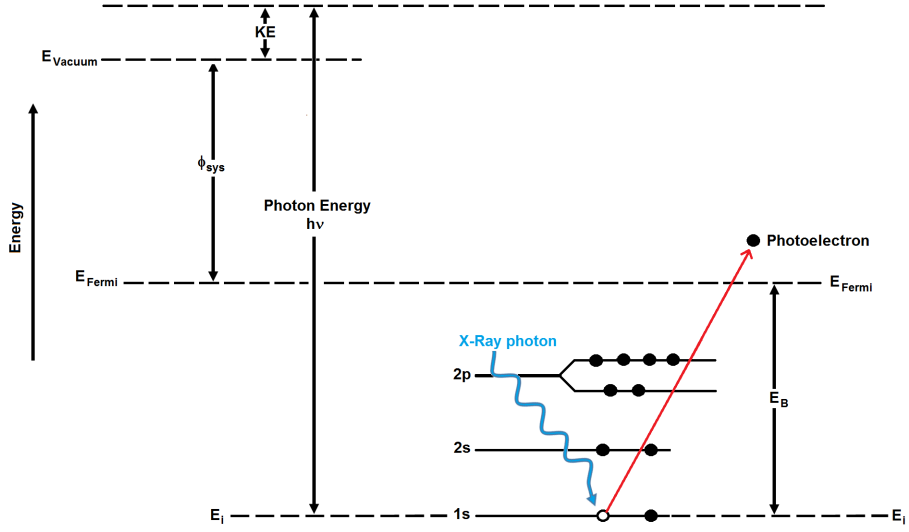


Figure 2.5: Schematic picture describing the photoelectron emission (right), and energy reference levels (left).

There can also exist secondary electrons than can be detected by the analyzer. Some of these are due to intra-atomic relaxation processes and are called Auger electrons [12,13]. An schematic picture of this process is shown in Fig. 2.6 [11,12]. In the Auger electron process, a higher level electron falls into a core level releasing some energy, this energy is transferred to another (secondary) electron in an equivalent or higher state giving the secondary electron enough energy to be sent into the vacuum, and then available to be detected by the analyzer. Auger electrons and photoelectrons can be distinguished because the kinetic energy of Auger electrons is independent of the energy of the incoming photon, while photoelectrons do depend the on photon's energy. These secondary electrons are used for other types of surface analysis but were not considered nor used in this work.

Apart from Auger electron features, the photoemission process will lead to mainly two different types of signals [12]: signal coming from ejected electrons which have not suffered energy loss due to inelastic collisions, and signal from electrons that have lost energy. The former will lead to a nice and well-defined peak in the spectrum, centered in the binding

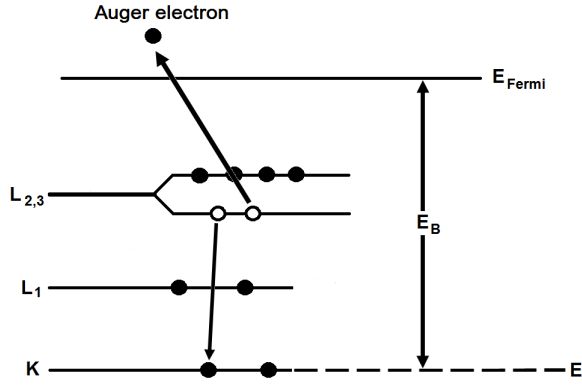


Figure 2.6: Schematic picture describing the Auger electron emission.

energy corresponding to the initial state, while the second one will increase the background of the signal. In this study, all XPS data were extracted and analyzed utilizing the CASA software package [14], and a Shirley background [13,15] was used and subtracted from the core level features.

XPS spectra were acquired using a dual anode X-ray lamp, XR 50 from SPECS, and a VG100AX 100 mm hemispherical analyzer (electron energy analyzer detector). The measurements were performed inside of a ultra-high vacuum (UHV) chamber ($\sim 10^{-10}$ Torr) to prevent impurity, and contamination contributions. The X-ray source used most commonly was the Mg-K α line at 1253.6 eV. Sample was placed in front of the analyzer, oriented such that the data is taken at normal emission, and X-rays hit the sample with an incident angle of 45° (Fig. 2.7c).

The XPS was used to characterize the Au interface with semiconducting boron carbide, and boron carbide samples containing the aromatic compounds. Gold deposition was also carried out in our UHV system, to aid in the fabrication of an interface free of impurities and contamination.

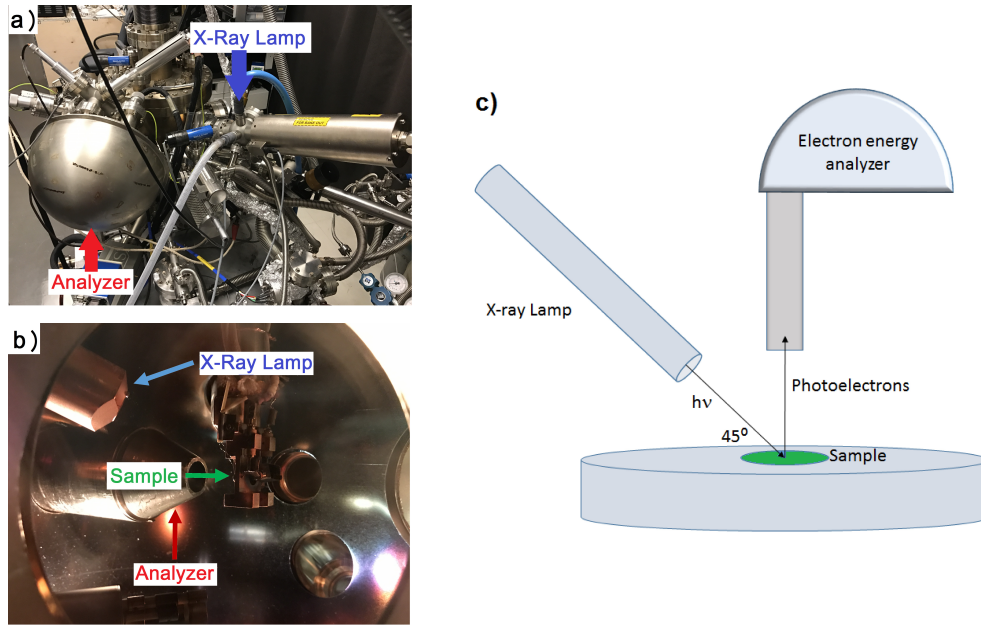


Figure 2.7: Left: Pictures of the equipment configuration for XPS at the University of Nebraska - Lincoln: a) outside and b) inside set up. Right: c) The geometrical set up of the elements for XPS.

Variable angle spectroscopic ellipsometry (VASE)

As was mentioned before, one of the key parameters for boron carbides applications is thickness. Thicker or thinner films will define if these semiconductor can or cannot be used in a particular application, such as neutron detection. Therefore, in order to characterize these devices, it is important to have a precise way to calculate the thickness of the samples, and VASE is a useful technique to achieve this. This technique is also commonly used as well to determine the band gap of the samples, as well as the optical constants as the refractive index (n) and dielectric constants (ϵ_1, ϵ_2) of the films; this is extremely important as this leads to a better characterization of the samples.

The optical experiments do not directly measure the quantities of interest, rather they measure changes in the reflected beam due to physical properties of the sample being studied. The key changes measured are the reflected or transmitted beam intensities and polarization

states. It is known that layer thickness, optical constants or any other structural parameter of the sample will affect the measured quantities, therefore analysis is needed, as a function of the photon energy, but it is possible to infer the values of the dielectric response, with a high precision, from the Δ and Ψ parameters being studied [16.17].

The VASE combines variable angle of incidence and spectroscopy measurements. The mathematical theory for VASE is based on Fresnel's boundary equations. It uses the reflection of polarized light from the material being studied and looks for changes in the angle of polarization as a function of photon energy. The ellipsometry measurements are expressed as Ψ and Δ , which are related to the ratio of the complex Fresnel reflection coefficients of the sample r_p and r_s as shown in equation 2.2.

$$\tan(\Psi)e^{i\Delta} = \rho = \frac{r_p}{r_s} \quad (2.2)$$

r_p and r_s are the coefficients for p- (in the plane of incidence) and s- (perpendicular to the plane of incidence) polarized light, respectively [16.17]. As VASE measures the ratio between these two quantities instead of their absolute value, it can be both highly accurate and sensitive. One advantage is that the detectors used in this technique do not need to be calibrated, which means that no reference sample or beam is needed. Additionally, as the incidence angle changes, the relative polarization, with respect to the surface/boundary, will be different providing new information about the sample compared to simple spectroscopic ellipsometry [17].

The data analysis was carried out by modeling the measured data as a function of the parameters of interest, and to estimate the parameters that best match the experimental data. A block diagram showing this procedure is shown in Fig. 2.8.

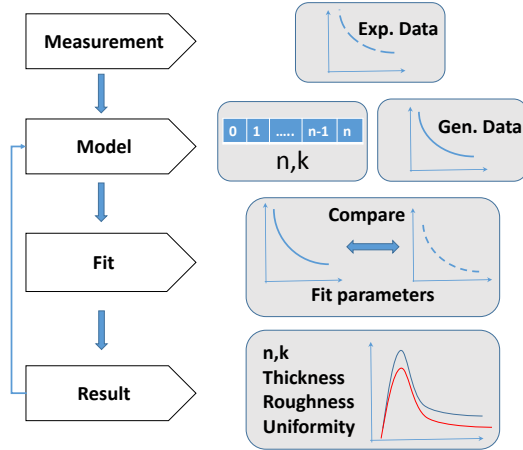


Figure 2.8: Basic procedure to determine some properties of a material being studied using VASE [16].

The process consists of basically four steps:

- 1) Measurements are taken
- 2) A model to fit the experimental data is proposed
- 3) Generated data from the model and experimental data are compared
- 4) If the results do not match, it is necessary to go back to the model and modify the values of the unknown parameters

Steps 2) and 3) are repeated until the best set of optimized parameters are found such that the generated data closely match the experimental data. In constructing the model it is necessary to have into account not only the parameters being investigated, but also known parameters from the experimental set up as the wavelength of the incident light, the incident beam polarization state, and the angle of incidence [17].

The ellipsometry data in this study² were acquired using multiple instruments, but primarily on a J A Woollam RC2 VASE ellipsometer in ambient conditions. Data were acquired from films deposited on SiO₂ substrates, over a range of photon energies in the visible to ultra-violet range 0.73 eV - 6.4 eV (1690 nm - 193 nm), in increments of 1 nm (1000 nm - 1690 nm) and 2.5 nm (1000 nm - 193 nm), respectively. The angles of incidence were varied from 45° to 75°, in 5° increments. Data were fit by standard methods [18-20], using commercially available software.

Band Gap Determination

VASE was also used to calculate the band gap of the boron carbide films. Being boron carbide amorphous material, it is appropriate to use the Tauc-Lorentz (TL) model [18-20]. In this model, the imaginary part of the dielectric function is determined using a combination of the Tauc Band edge and the Lorentz formulation for a collection of uncoupled atoms. The mathematical expression for the imaginary part of the dielectric function is given by equation 2.3.

$$\epsilon_2^{TL} = \begin{cases} \frac{AE_0C(E-E_g)^2}{(E^2-E_0^2)^2+C^2E^2} \frac{1}{E} & E > E_g \\ 0 & E \leq E_g \end{cases} \quad (2.3)$$

where E_0 is the peak transition energy (Lorentz resonant energy) and C is the Lorentz broadening parameter [18]. The amplitude and band gap energy are denoted by A and E_g , respectively.

² Optical measurements were carried out in collaboration with Dr. Tino Hofmann group at University of Nebraska - Lincoln, Department of Electrical and Computer Engineering.

Electrical and Transport Measurements

Current-voltage and capacitance-voltage measurements were used to determine the carrier (hole) lifetimes of the samples³. Diode detectors were formed by depositing Ti-Au electrodes, of area 2 mm x 2 mm, on each side of the heterojunction diodes. Electrical characterization is comprised of capacitance versus voltage, C(V), measurements and current versus voltage, I(V), measurements. The C(V) measurements were acquired using an HP Model 4192A Impedance Analyzer with an oscillation voltage set to 0.010 V, at set frequencies increased by decades from 1 kHz to 10 MHz in a 4 point parallel circuit. The I(V) measurements were obtained using a Keithley 2411B SourceMeter to deliver a dc voltage, a Keithley 6485 PicoAmmeter to measure the resulting current, and a HP 3478A multimeter to measure the voltage across the device under load [6,8,9].

The magnetoresistance (MR) curves were obtained by fixing the applied bias, and running a sweep scan of the current across the film surface as a function of the applied external magnetic field on the thin films, which have an estimated film thickness of 90-200 Å. I-V curves for these films were carried out using a Keithley 236 source and plotted as a function of the in-plane external magnetic field. Samples were placed in a simple cryogenic system, and a magnetometer was used to generate fields ranging from -1 T up to +1 T, as shown in Fig. 2.9. All transport measurements were carried out at room temperature.

³ Carrier lifetimes were determined from this data by George Peterson.

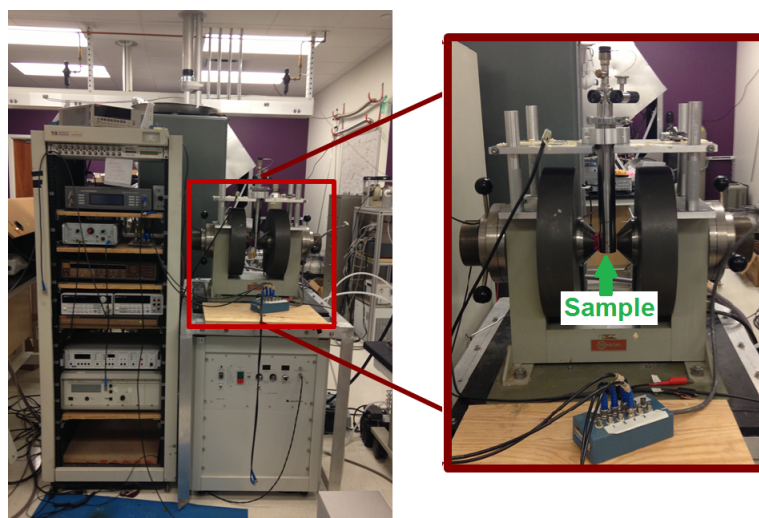


Figure 2.9: Equipment for magnetoresistance measurements at the University of Nebraska - Lincoln. Right: The combination of cryogenic system with the magnet, although the key measurements were at room temperature.

References

- [1] Pasquale, F.L., Lui, J., Dowben, P.A., Kelber, J.A. Novel semiconducting alloy polymers formed from *ortho*-carborane and 1,4-diaminobenzene. *Materials Chemistry and Physics* **133** (2012) 901-906
- [2] Pasquale, F.L., Li, Y., Du, J., and Kelber, J.A. Novel alloy polymers formed from *ortho*-carborane and benzene or pyridine. *J. Phys.: Condens. Matter* **25** (2013) 105801
- [3] Robinson, J., Pasquale, F.L. and Kelber, J.A. Plasma-enhanced chemical vapor deposition of *ortho*-carborane: structural insights and interaction with Cu overlayers. *J. Phys.: Condens. Matter* **25** (2013) 355004
- [4] Planas, J.G., Teixidor, F., Viñas, C. N,O-Type Carborane-Based Materials. *Crystals* 2016, 6(5), 50; doi:10.3390/crust6050050.
- [5] Pasquale, F.L., Kelber, J.A. Site-specific electron-induced cross-linking of *ortho*-carborane to form semiconducting boron carbide. *Applied Surface Science* **258** (2012) 2639-2642
- [6] Echeverria, E. et al., Significant magneto-resistive effects in boron carbide thin films. *Materials Letters* **110** (2013) 20-23

- [7] Dong, B., James, R., Kelber, J.A. PECVD of boron carbide/aromatic composite films: Precursor stability and resonance stabilization energy. *Surface & Coatings Technology* **290** (2016) 94-99
- [8] Echeverria, E. et al., Novel semiconducting boron carbide/pyridine polymers for neutron detection at zero bias. *Appl. Phys. A*, Vol. **118** issue 1 (2014) 113-118.
- [9] Echeverria, E. et al., Semiconducting boron carbides with better charge extraction through the addition of pyridine moieties. *J Phys D Appl Phys* **49** (2016) 355302
- [10] Schlaf, R. Calibration of Photoemission Spectra and Work Function Determination. Retrieved from <http://rsl.eng.usf.edu/Documents/Tutorials/PEScalibration.pdf>
- [11] Chusuei, C.C., and Goodman, D.W., X-Ray Photoelectron Spectroscopy. *Encyclopedia of Physical Science and Technology* **17** (2002) 921-938
- [12] Briggs, D. et al., *Handbook of X-ray Photoelectron Spectroscopy*, Perkin-Elmer Corp., Physical Electronics Division, Eden Prairie, Minnesota, USA, 1979.
- [13] Colón Santana, J.A.(2015) Quantitative Core Level Photoelectron Spectroscopy: A Primer. Morgan and Claypool Publishers, California, USA.
- [14] Fairly, N. CasaXPS: processing software for XPS, AES, SIMS and More. Retrieved from <http://www.casaxps.com>
- [15] Végh, J. The Shirley background revised, *J. Electron Spectrosc. Relat. Phenom.* **151** (2006) 159
- [16] A Short Course in Ellipsometry. J.A. Woollam Co., Inc. 2001
- [17] Woollam, J.A., Johs, B., Herzinger, C.M, Hilfiker, J., Synowicki, R., Bungay, C.L. Overview of Variable Angle Spectroscopic Ellipsometer (VASE), Part I: Basic Theory

and Typical Applications. Proceedings of Optical Science and Technology. (1999)
VolCR72

- [18] Jellison, G.E. Spectroscopy ellipsometry data analysis: measured versus calculated quantities. *Thin Solid Films.* (1998) **313-4** 33
- [19] Ahmad, A.A., Ianno, N.J., Snyder, P.G., Welipitiya, D., Byun, D. and Dowben, P.A. *J. Appl. Phys.* (1996) **79** 8643
- [20] Fujiwara, H. (2007) Spectroscopic Ellipsometry: Principles and Applications, John Wiley & Sons, Ltd, Chichester, UK. doi: 10.1002/9780470060193

Chapter 3

GOLD (Au) CONTACTS

Introduction

In characterizing semiconductor devices, one essential parameter is the kind of contact created at the interface when a metal is deposited on the semiconductor. Therefore, this chapter is dedicated to show how gold (Au) deposition interacts with the novel boron carbide-based semiconductors. Some of the results presented in this chapter were published in [1,2].

As mentioned in section 2.3, X-ray photoemission spectroscopy has been used to investigate the interaction of Au with these novel boron carbide-based semiconductors. The electronic structure has also been investigated by valence band photoemission. Both n- and p-type samples have been tested and pure boron carbide devices are compared to those containing aniline and pyridine.

In this chapter the basic theory of metal-semiconductor contacts is discussed in the context of ideal contacts, and then results obtained with Au deposition on pure boron carbide and doped boron carbide is presented.

Metal-Semiconductor Contacts: Theory

When a metal is deposited on the surface of a semiconductor device, it can act as either a rectifying contact (Schottky barrier diodes) or as a non-rectifying contact (ohmic contact).

An ideal contact deposition is characterized by the following three features[3]:

1. There is not any additional layer between the metal and the semiconductor, i.e., the metal and the semiconductor are in direct contact on the atomic scale¹.
2. No interdiffusion or intermixing effects are present².
3. It is assumed that there are no surfaces charges or adsorbed impurities on the interface³.

As the band structure for a metal is different than the one for the semiconductor, it is needed to introduce a new energy level from which all energies will be referenced, it is the vacuum energy level (E_{vacuum} or E_0). This energy represents the energy needed to free an electron away from the solid [4]. Fig. 3.1 shows the energy bands diagrams for an isolated metal and an isolated semiconductor, the vacuum energy level is label as E_0 .

There are several terms to keep in mind from the diagrams shown in Fig. 3.1, one of them is the work function Φ . This is the energy difference from the vacuum energy and the Fermi energy (E_F) of the material. In the case of the metal, this quantity is a fundamental property. For Au its value is 4.8 eV. For semiconductors, the Fermi energy level (E_{FS}) depends

¹ All of the samples used for this study were cleaned by Ar^+ sputtering, therefore any oxide surface is eliminated before the Au deposition. Additionally, samples were kept in ultra high vacuum, without exposure to ambient conditions.

² Au layers were removed by Ar^+ sputtering after the last Au deposition on each sample. XPS data did not show Au diffusion, as will be discussed later in this chapter.

³ All depositions and measurements were carried out in ultra high vacuum to assure an interface free of impurities and contamination.

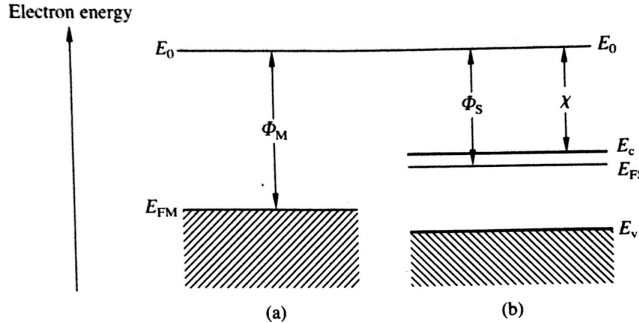


Figure 3.1: Energy band diagram for a) metal a b) n-type semiconductor. Taken from [4].

on the doping of the material rather than the material itself, hence, the work function of the semiconductor (Φ_S) will depend on the doping as well. Consequently, it is needed to define a new term that counts as a fundamental property of the semiconductor. This quantity is called *electron affinity* energy (χ), and corresponds to the energy difference from the vacuum level to the conduction band edge of the semiconductor (E_C).

When the metal is placed in perfect contact with the semiconductor, charges will be transferred from one side to the other until equilibrium is reached and Fermi levels are aligned [5]. The electron's transfer will depend on the type of the semiconductor (n-type or p-type) and the difference between the work function of the metal (Φ_M) and the semiconductor (Φ_S). There exist four cases to be considered:

- 1) n-type semiconductor and $\Phi_M > \Phi_S$
- 2) p-type semiconductor and $\Phi_M < \Phi_S$
- 3) n-type semiconductor and $\Phi_M < \Phi_S$
- 4) p-type semiconductor and $\Phi_M > \Phi_S$

Schottky Barrier Diodes

Consider the case shown in Fig. 3.1, $\Phi_M > \Phi_S$ and n-type semiconductor. When the metal is brought in direct contact with the semiconductor, electrons from the semiconductor will transfer to the metal in order to align their energy Fermi level. In doing this, the surface of the semiconductor will be depleted (see Fig. 3.2), similar to the case of n-p junctions, and an electric field will be created in this region. This electric field will apply a force to the carriers that is opposite of the direction of the carrier diffusion, thus preventing further net electron diffusion from the semiconductor. Note that either the work function of the metal or the electron affinity cannot be modified just by placing these two materials together, as they are fundamental properties of each material.

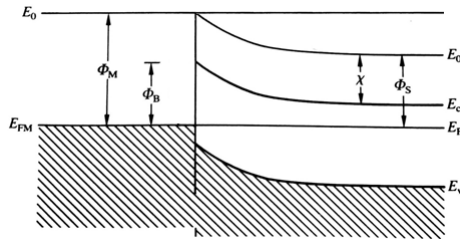


Figure 3.2: Energy band diagram for a Schottky barrier. Taken from [4].

After the system reaches thermal equilibrium, the electrons in the metal with energy equal to the Fermi energy (E_{FM}) will see a potential barrier, Φ_B , which will prevent them to move into the conduction band of the semiconductor. This potential barrier is called Schottky barrier and can be calculated by eq. 3.1.

$$\Phi_B = \Phi_M - \chi \quad (3.1)$$

Similarly, electrons in the conduction band of the semiconductor will see a contact potential (V_0) towards the metal, which is the difference between the work function of the metal and the work function of the semiconductor, $V_0 = \Phi_M - \Phi_S$ [5]. This kind of contacts is

also called a rectifying contact, because due to the Schottky barrier, the current will flow easily from one direction but not in the other when an external voltage is applied [4].

If the semiconductor is grounded and a positive voltage is applied to the metal, the barrier seen by electrons in the semiconductor will decrease allowing them to move into the metal, therefore generating a current through the device. On other hand, applying a negative voltage will increase the barrier on the surface blocking the flow of electrons from the semiconductor [3].

A similar situation occurs when a p-type semiconductor is in direct contact with a metal which has a smaller work function compared to the semiconductor, i.e., $\Phi_M < \Phi_S$. Fig. 3.3 shows the energy band diagram for this situation.

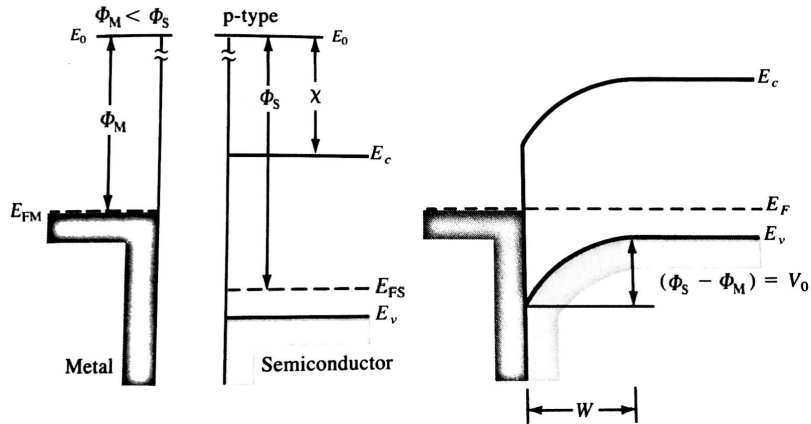


Figure 3.3: Energy band diagram for p-type semiconductor when $\Phi_M < \Phi_S$. Left: Isolated energy bands for the metal and the semiconductor, Right: Thermal equilibrium. Modify from [5].

In this situation, the holes in the p-type semiconductor see a barrier, $V_0 = \Phi_S - \Phi_M$, towards the metal. On other hand, electrons in the metal will see a barrier when flowing to the semiconductor. If a voltage is applied, the barrier will decrease or increase depending on the polarity of the applied voltage. As a result, a Schottky barrier diode is formed.

Ohmic Contacts

Now, consider a n-type semiconductor placed in a direct contact with a metal for which $\Phi_M < \Phi_S$, as shown in Fig. 3.4.

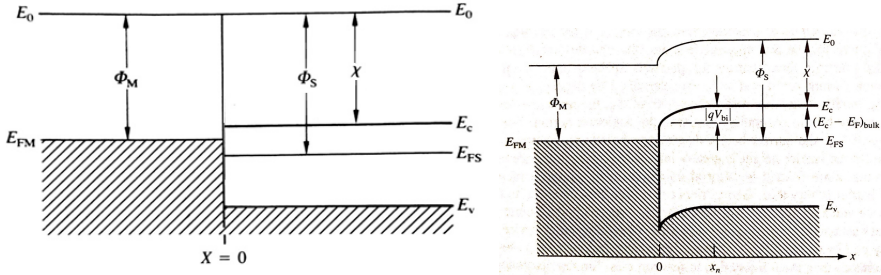


Figure 3.4: Energy band diagram for n-type semiconductor when $\Phi_M < \Phi_S$. Left: Non-equilibrium situation, Right: Thermal equilibrium. Taken from [4].

The Fermi level of the metal is in a higher position than the Fermi level for the semiconductor, as a result, upon direct contact, electrons will flow from the metal into the semiconductor until thermal equilibrium is reached. Although there is a band bending in the semiconductor, this bending is downwards at the surface, therefore electrons do not see any barrier as in the case of the Schottky barrier diode. Any positive applied voltage will lead to a current from the semiconductor to the metal. In the case of the electrons on the metal, they still see a small barrier, but it will be vanished with a reverse applied voltage [3]. This behavior is not rectifying, but instead is like having a resistor, accordingly, this type of contacts is called ohmic.

Finally, let us consider the case where a p-type material is placed in direct contact with a metal such that $\Phi_M > \Phi_S$, as shown in Fig. 3.5. The Fermi energy level of the semiconductor is higher than the one for the metal, hence, electrons will move from the semiconductor to the metal. At thermal equilibrium, there will be a band bending on the surface of the semiconductor, but this band bending is not going to affect the flow of electrons when a

voltage is applied to the device. As a result, an ohmic contact is formed.

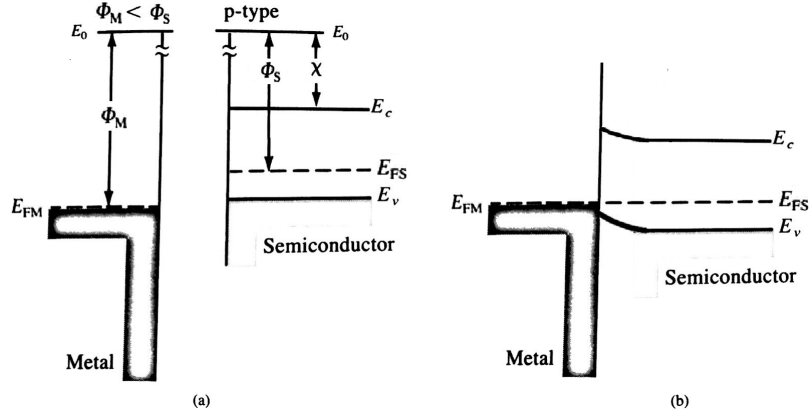


Figure 3.5: Energy band diagram for p-type semiconductor when $\Phi_M > \Phi_S$. a) Non-equilibrium, and b) Thermal equilibrium. Modify from [4].

In conclusion, when a metal is in ideal contact with a semiconductor, there exist two configurations that lead to Schottky barrier diodes: a) n-type semiconductor with $\Phi_S < \Phi_M$, and b) p-type semiconductor with $\Phi_S > \Phi_M$. The other two situations (n-type semiconductor and $\Phi_M < \Phi_S$; p-type semiconductor and $\Phi_M > \Phi_S$) will lead to an ohmic contacts.

Now, let us discuss the results for the metal/semiconductor interface in the case of boron carbide based semiconductors.

Au/Boron Carbide Based Semiconductors

Understanding of the metal contacts on the surface of boron carbide samples is not a new topic in the world of semiconductor devices [6-9]. However, so far there are no reports investigating Au deposition for boron carbide based devices. Investigating the interaction of Au with semiconducting boron carbide is therefore a natural extension of efforts to understand how to optimize the contacts to PECVD boron carbide devices.

While semiconducting boron carbides are generally p-type, in the absence of transition metal doping [10-14], semiconducting boron carbides made by the plasma enhanced chemical vapor deposition (PECVD) from metacarborane (the closo-1,7-dicarbadodecaborane isomer of the icosahedral closo-carboranes, $C_2B_{10}H_{12}$) are generally n-type [14-17]. In this work, deposition of Au on both n- and p-type semiconductors were studied. Subsequently, both precursors (1,2 dicarbadodecaborane and 1,7 dicarbadodecaborane) were used. Samples formed by PECVD from *ortho*-carborane will be labeled as *o*-BC, and those based on *meta*-carbonare will be m-BC.

To reduce any oxide layer on the surface of the semiconductor, all films were cleaned prior to Au deposition by Ar^+ bombardment at $\sim 9.5 \times 10^{-5}$ Torr at 1.0 kV. To maximize the uniformity of the reduced surface layer, samples were rotated $\pm 40^\circ$ off normal, with respect to the incident ion beam, during each sputtering cycle.

XPS measurements were carried out after each sputtering, and cycles of sputtering followed by XPS were repeated until non-significant changes were seen in the oxygen signal. Accordingly, times of sputtering were varied from 15 min to 45 min. The Au was deposited via thermal evaporation from a tungsten (W) filament basket at a pressure of 10^{-7} Torr. Different Au coverages ranging from 4 Å to 27 Å average thickness, as determined by XPS, were investigated.

To avoid any contamination or oxide formation at the surface, the sample was transferred to the photoemission chamber, after each Au deposition, without exposure to ambient conditions. Ar^+ bombardment was also used to remove deposited Au from the films surface to determine the reversibility of the surface interactions. During the sputtering process, the same Ar pressure and beam voltage conditions were used as for initial surface cleaning.

Different Ar⁺ ion sputtering times, however, running from 15 min to 1 h, were selected in order to eliminate more Au layers.

***ortho*-carborane based Samples**

In this section two types of *o*-BC will be discussed, pure boron carbide (*o*-BC) and boron carbide with aniline (*o*-BC:Aniline). First, results from XPS analysis of the film before and after of the Ar⁺ sputter cleaning will be discussed, and then results of Au deposition will be presented.

Before Au Deposition

Table 3.1 compiles the chemical composition before and after the cleaning process for both samples. For the case of *o*-BC, oxygen content increases as the film is cleaned, while carbon content decreases, meaning that this sample has large oxygen content on the bulk, and there were some carbon contamination on the surface of the sample. In the case of *o*-BC:aniline film, oxygen contamination was reduced with Ar⁺ sputtering, but there was still some oxygen in the bulk of the sample or on the sample platten (thus having nothing to do with the boron carbide samples). The boron carbide with aniline contains lower apparent oxygen content compared to *o*-BC film. These values do not reflect the presence of hydrogen in the samples because hydrogen cannot be detected by XPS. Therefore, our results will be limited to the information obtained from boron, carbon, oxygen and nitrogen signals.

It can be seen that the sample containing aniline has higher carbon content compared to the pure boron carbide; this is expected as aniline is made of carbon rings, as seen in Fig

	Film	Boron	Carbon	Oxygen	Nitrogen
Before cleaning	<i>o</i> -BC	42.6%	41.2%	16.2%	–
	<i>o</i> -BC:aniline	19.3%	62.6%	13.6%	4.5%
After cleaning	<i>o</i> -BC	47.7%	32.7%	19.6%	–
	<i>o</i> -BC:aniline	20.9%	64.5%	9.2%	5.4%

Table 3.1: Chemical composition of the pure boron carbide (*o*-BC) film and the pure boron carbide and aniline (*o*-BC:aniline) film as determined by XPS.

2.2d in section 2.2. The measured binding energies for the B(1s), C(1s), O(1s) and N(1s) core levels associated with each film are summarized in table 3.2. These values are in good agreement with previous results [6-9,18,19].

Film	B(1s) eV	C(1s) eV	O(1s) eV	N(1s) eV
<i>o</i> -BC	190.8	285.1	533.8	–
<i>o</i> -BC:aniline	190.3	284.9	532.9	399.3

Table 3.2: XPS measured binding energies for B(1s), C(1s), and N(1s) core levels for the pure boron carbide (*o*-BC) film and the pure boron carbide and aniline (*o*-BC:aniline) film.

Each core level spectrum can be deconvoluted into different peaks depending on the molecular structure of the films: each peak represents one bonding environment on this structure. However, it is not always possible to distinguish all of the features due to the small difference between binding energies, the resolution of the system, and/or the complexity of these multiple bondings. For instance, peaks representing direct hydrogen bonds (e.g. B-H, C-H, etc) are not discernible as hydrogen is not detected by XPS as was mentioned before. In the case of carbon for instance, binding energies related to carbon oxides, C_xO_y (with different values for x and y), are difficult to recognize. Consequently, for the goal of this work, only deconvolution into peaks representing the main bonds in each structure will be considered.

Figure 3.6 shows the spectra for the B(1s), C(1s), and O(1s) core levels, and their corresponding components, for the *o*-BC film. In the case of B(1s), its spectrum can be deconvoluted into four main peaks, as seen in Fig. 3.6 top left. The two lowest binding energy components correspond to B-B bonding environments (188.8 eV/ 190.3 eV), the next high energy (191.9 eV) represents B-C species, and finally the last component at the highest binding energy (193.6 eV) belongs to boron oxides.

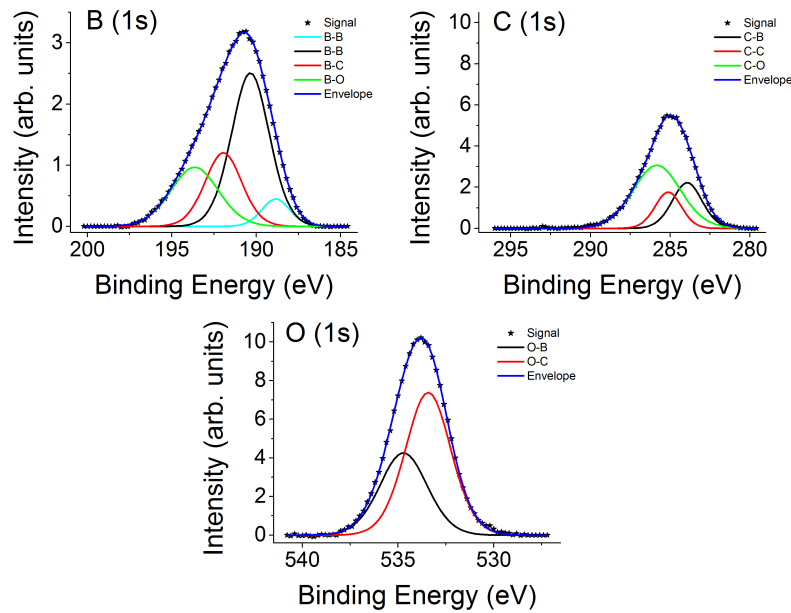


Figure 3.6: Deconvoluted XPS spectra of the B(1s), C(1s) and O(1S) core levels for the pure boron carbide film, *o*-BC.

From Fig. 2.1 in section 2.2, it is clear that there are more B-B species than B-C, this is evident in the spectrum for B(1s) core level (Fig. 3.6) as the intensity (and area) for B-B bonding environments is larger than for the B-C species. Additionally, there are two types of B-B bonding environments clearly distinguishable in the spectrum, although the one at lowest binding energy has low intensity.

In the case of the C(1s) core level, the spectrum is composed of three main peaks, one at 293.9 eV corresponding to C-B species, a second one at 285.1 eV representing C-C species, and the last one at 285.8 eV due to carbon oxides. C-C bonding environments are expected as *ortho*-carborane precursors were used in the fabrication of this film. For O(1s) core level, there are two main components: oxygen bonded with carbon at 533.4 eV, and oxygen bonded with boron at 534.7 eV. As it is seen in the O(1s) spectrum in Fig. 3.6 bottom, most of the oxygen is bonded to carbon elements. This is confirmed from the C(1s) spectrum in the same figure, as the intensity for C-O is also high compared to the other peaks. From these results it can be inferred that oxygen contamination comes from the growth process.

A similar process was done for the *o*-BC:aniline film. Figure 3.7 shows the deconvoluted spectra for B(1s), C(1s), N(1s) and O(1S). The B(1s) core level in this case is deconvoluted into three main peaks: one at 188.7 eV which represents the B-B species, other at 190.3 eV representing B-C bonds, and the last one for boron oxides at 192.1 eV. The aromatic/*ortho*-carborane ratio for this sample is 3:1, hence, it makes sense to have a large concentration of B-C bonds compared to B-B, and only one appreciable B-B bonding environment.

The C(1s) core level, on other hand, can be deconvoluted into 5 different peaks, one more peak is present compared to the *o*-BC film. The additional peak represents C-N bonds, and is located at 286.0 eV. C-B and C-C bonds are located at similar positions as before, 283.8 eV and 284.9 eV respectively. The last peak can be attributed to carbon oxides (288.2 eV).

On other hand, the O(1s) core level is composed of three different peaks. Similar as for the case of pure boron carbide, there is one peak representing oxygen bonded with boron, at 533.4 eV, and one for oxygen bonded with carbon, at 532.6 eV. The binding energies

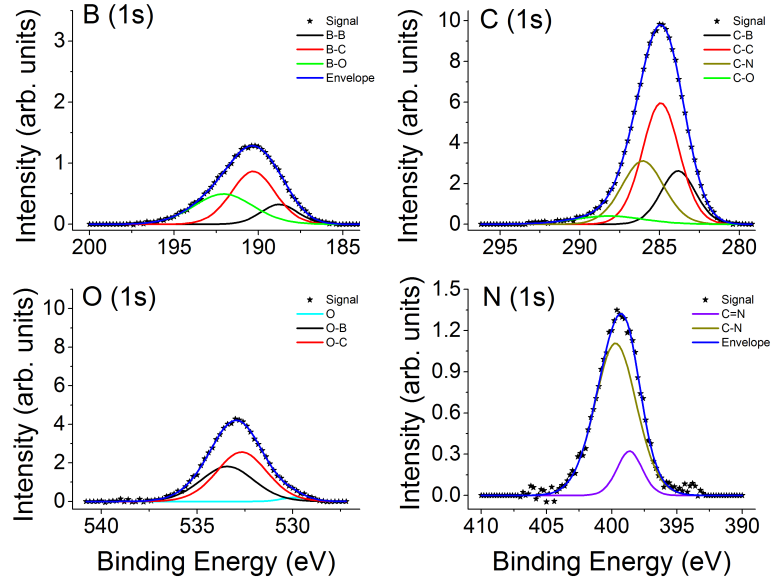


Figure 3.7: Deconvoluted XPS spectra of the B(1s), C(1s), O(1s) and N(1s) core levels for the boron carbide with aniline film, *o*-BC:aniline.

for these bonding environments are however higher than these of the pure boron carbide. There is one more peak in this spectrum at 529.9 eV. This peak cannot be associated to oxygen bonded to nitrogen as the binding energy is too far from that corresponding to this type of bonds (around 533 eV). As the binding energy for this third peak is very close to that of the natural form of oxygen, this peak is assigned to small oxygen contamination on the surface of the film.

Deconvolution of the N(1s) core level leads to two different peaks. The peak located at 398.6 eV represents C=N bond, while the one at 399.7 eV is related to C-N bond. Due to the fact that nitrogen signal is coming from the aniline moieties, and that the aromatic compounds are linked to the boron carbide through C-B bonds (see Fig. 2.3 in section 2.2.1), it is not expected to have any nitrogen bonded to boron, therefore no peaks on B(1s) or N(1s) core levels representing B-N are present, as is seen in Fig. 3.7. No nitrogen oxides are seen

either.

All of the binding energy values reported in this section are in good agreement with those found in the literature, see for instance [6-9,18,21].

After Au Deposition

As gold was deposited on the surface of the semiconductor, the binding energy of each element is moved toward high values, as shown in Fig. 3.8 for the *o*-BC, and Fig. 3.11 for the *o*-BC:aniline film⁴. The shift in binding energy for the *o*-BC sample in the case of B(1s) core level is (2.2 ± 0.5) eV, while for the *o*-BC:aniline film it is (7.7 ± 0.7) eV.

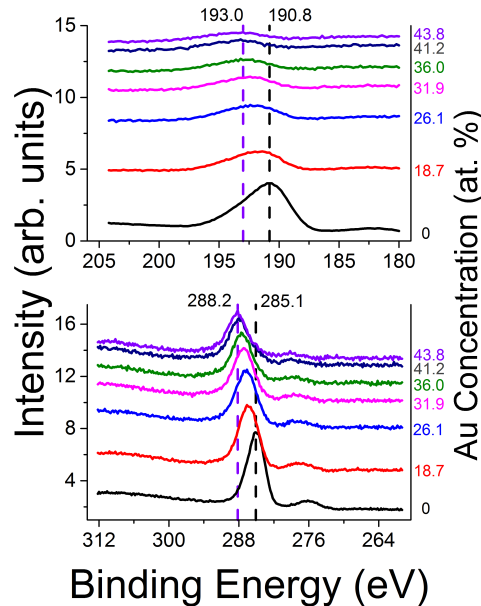


Figure 3.8: XPS core level spectra of the B(1s) (Top), and C(1s) (bottom) as a function of the Au deposition for the pure boron carbide (*o*-BC) film.

⁴ Only B(1s) and C(1s) core levels are presented for clarity, however, a shift in the binding energies of O(1s), N(1s) and Au(4f) core levels was seen as well.

Semiconductor devices formed by PECVD from *ortho*-carborane are p-type. Being the work function of the Au larger than the work function of the boron carbide, it is expected that ohmic contacts are formed, as discussed in section 3.2.2. Consequently, no change or smaller binding energies are expected for the metal/semiconductor contacts. However, a shift to high binding energies is observed as Au is deposited on the sample, therefore, a Schottky barrier is formed in the interface between Au and the boron carbide based semiconductors.

On other hand, intensities of the main core levels decrease as Au layers increase. Being XPS a surface sensitive technique, it is expected to see more and more Au layers while the signal for the other elements on the sample will decrease relative to the clean spectra. However, it is also an indication that no Au diffusion, or oxide layers are formed during the Au deposition, as reported in previous studies where Cr, Ti, and Al metals were used [6]. Oxide layers or metal diffusion will affect the metal/semiconductor interface as mentioned in section 3.2.

Table 3.3 summarizes the relative atomic concentration of each element in both samples, *o*-BC and *o*-BC:aniline, determined by XPS⁵. In the case of the *o*-BC film, changes in the relative atomic concentration are more drastic for boron, and oxygen, meaning that these elements are more constricted to the bulk of the film compared to the surface. With some Au depositions, the relative atomic concentration of C increases slightly, and a small feature is seen in the deconvoluted spectra for C(1s) at high binding energies (Fig. 3.9 right). No additional features are seen in the B(1s) spectra⁶. These results suggest that, in the case of *o*-BC, gold interacts with carbon species more strongly than with boron.

⁵ These values represent the atomic concentration on the top of the sample, of the order of tens of angstroms, since XPS is surface sensitive.

⁶ Although it is not shown here, no feature is seen in the O(1s) core level either.

Film	Gold	Boron	Carbon	Oxygen	Nitrogen
<i>o</i> -BC	0 %	47.7 %	32.6 %	19.7 %	–
	18.7 %	28.4 %	41.1 %	11.8 %	–
	21.6 %	24.6 %	39.5 %	9.8 %	–
	31.9 %	21.8 %	38.0 %	8.3 %	–
	36.0 %	19.4 %	36.3 %	8.3 %	–
	41.2 %	15.5 %	37.3 %	6.0 %	–
	43.8 %	15.0 %	35.6 %	5.6 %	–
<i>o</i> -BC:aniline	0 %	20.9 %	64.6 %	9.3 %	5.2 %
	14.4 %	11.9 %	63.3 %	7.3 %	3.1 %
	20.5 %	13.5 %	54.4 %	6.9 %	4.8 %
	24.7 %	12.4 %	53.4 %	5.4 %	4.1 %
	25.8 %	12.5 %	52.3 %	5.9 %	3.4 %

Table 3.3: Relative atomic concentrations obtained by XPS for gold, boron, carbon, oxygen and nitrogen.

The evolution of the deconvoluted B(1s) spectra (Fig. 3.9 left) with Au deposition shows a decreasing in the signal coming from the boron oxides, confirming that the oxygen contamination belongs to the bulk of the sample, therefore, it is due to the growth process. The B-C species became stronger than the B-B species with high concentration of Au (> at. 20%). Consequently, the C-B species in the C(1s) spectra became more stronger than the C-C species.

Fig. 3.10 shows the B(1s), C(1s) and O(1s) spectra after the last Au deposition, along with the deconvoluted peaks. In the O(1s) spectrum, only one peak is seen, corresponding to carbon oxides, which is in agreement with the third peak present in the C(1s) spectrum (at 289.4 eV). In this figure, the feature in the C(1s) core level, due to Au-C interactions, mentioned before is clearly seen.

For the sample containing aniline (*o*-BC:aniline) the change in binding energy (Fig. 3.11)

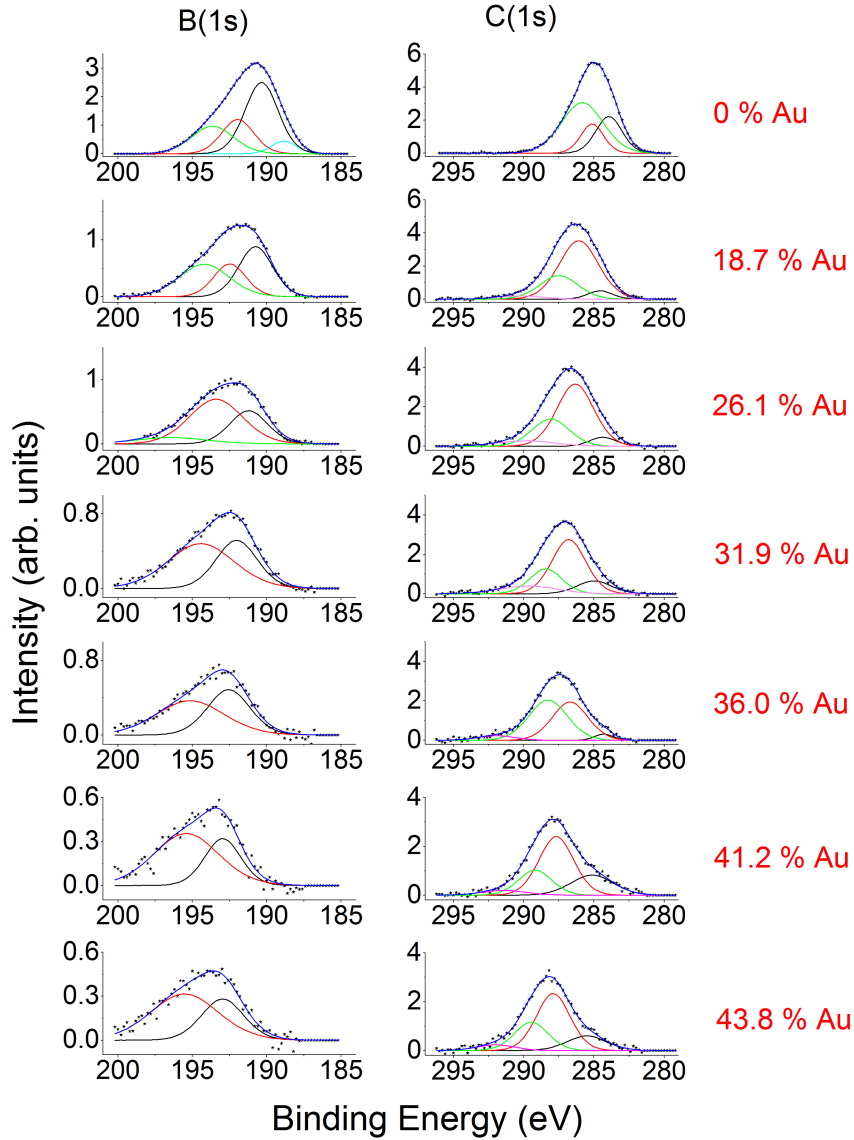


Figure 3.9: Evolution of the deconvoluted core level spectra of the B(1s) (left), and C(1s) (right) as a function of the Au deposition for the pure boron carbide (*o*-BC) film.

is more significant than the one for the pure boron carbide sample. The shift seen in both samples cannot be a photovoltaic charging effect, because the binding energy increases as the surface is metallized, which would lead to a decrease in binding energy if there was a significant suppression of the photovoltaic charging. Table 3.4 compile the change in binding energy for each element in each sample.

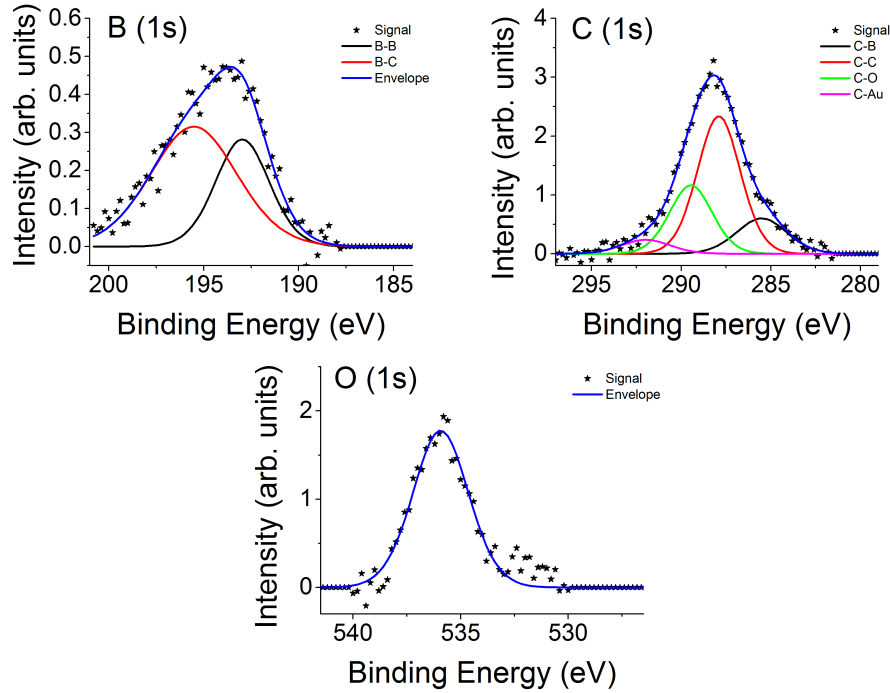


Figure 3.10: Deconvoluted XPS spectra of the B(1s), C(1s), and O(1s) core levels for the pure boron carbide (*o*-BC) film.

Film	Boron (eV)	Carbon (eV)	Oxygen (eV)	Nitrogen (eV)
<i>o</i> -BC	2.4 ± 0.5	3.1 ± 0.9	1.9 ± 0.2	–
<i>o</i> -BC:aniline	7.7 ± 0.7	6.8 ± 0.9	6.5 ± 0.5	6.7 ± 0.3

Table 3.4: Binding energy shift for all elements present in each sample, pure boron carbide (*o*-BC) and boron carbide plus aniline (*o*-BC:aniline).

As it was mentioned before, the atomic composition of boron is smaller for the sample containing aniline compared to the pure boron carbide, hence, less amount of Au was needed to analyze the metal/semiconductor interface⁷ (See table 3.3).

⁷ As one of the key components of the sample is boron, Au deposition was carried out in such way that being the signal for B(1s) core level small, it was still possible to get information about its main bonding environments, i.e. B-C and B-B species.

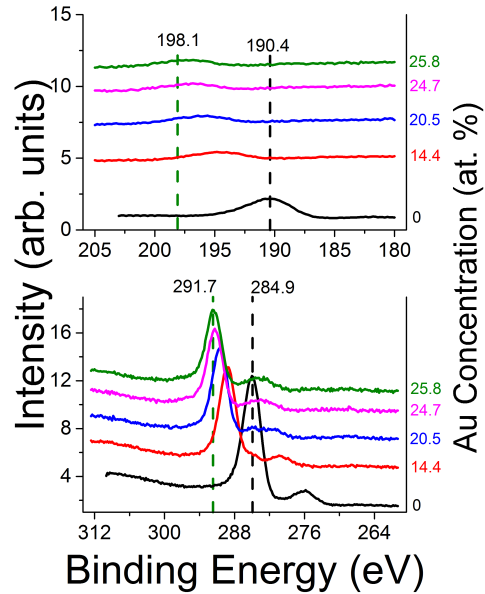


Figure 3.11: XPS core level spectra of the B(1s) (Top), and C(1s) (bottom) as a function of the Au deposition for the boron carbide with aniline (*o*-BC:aniline) film.

Fig. 3.12 shows the evolution of the B(1s), C(1s) and N(1s) core levels with Au deposition, as well as their main bonding environments. No feature indicating Au-C interactions is seen in this sample. This is consistent with the decreasing of the relative atomic concentration for carbon with Au deposition seen in table 3.3.

In this sample, the Au deposition is seen to modify the nitrogen signal. A small feature is seen with Au deposition, however it disappears with high Au relative atomic concentrations (> 25 %). This feature is seen at 407.8 eV with the first deposition, and it moves to higher binding energies with increasing Au content. It cannot be related to nitrogen oxides, since the spectra for O(1s) (not shown here) do not present any additional peak corresponding to oxygen bonding with nitrogen. Thus, this feature is assigned to Au-N interactions.

In the case of boron, no additional features are seen in the B(1s) core level spectra (Fig. 3.12 right), but changes in intensities in the B-B and B-C species are seen with Au deposi-

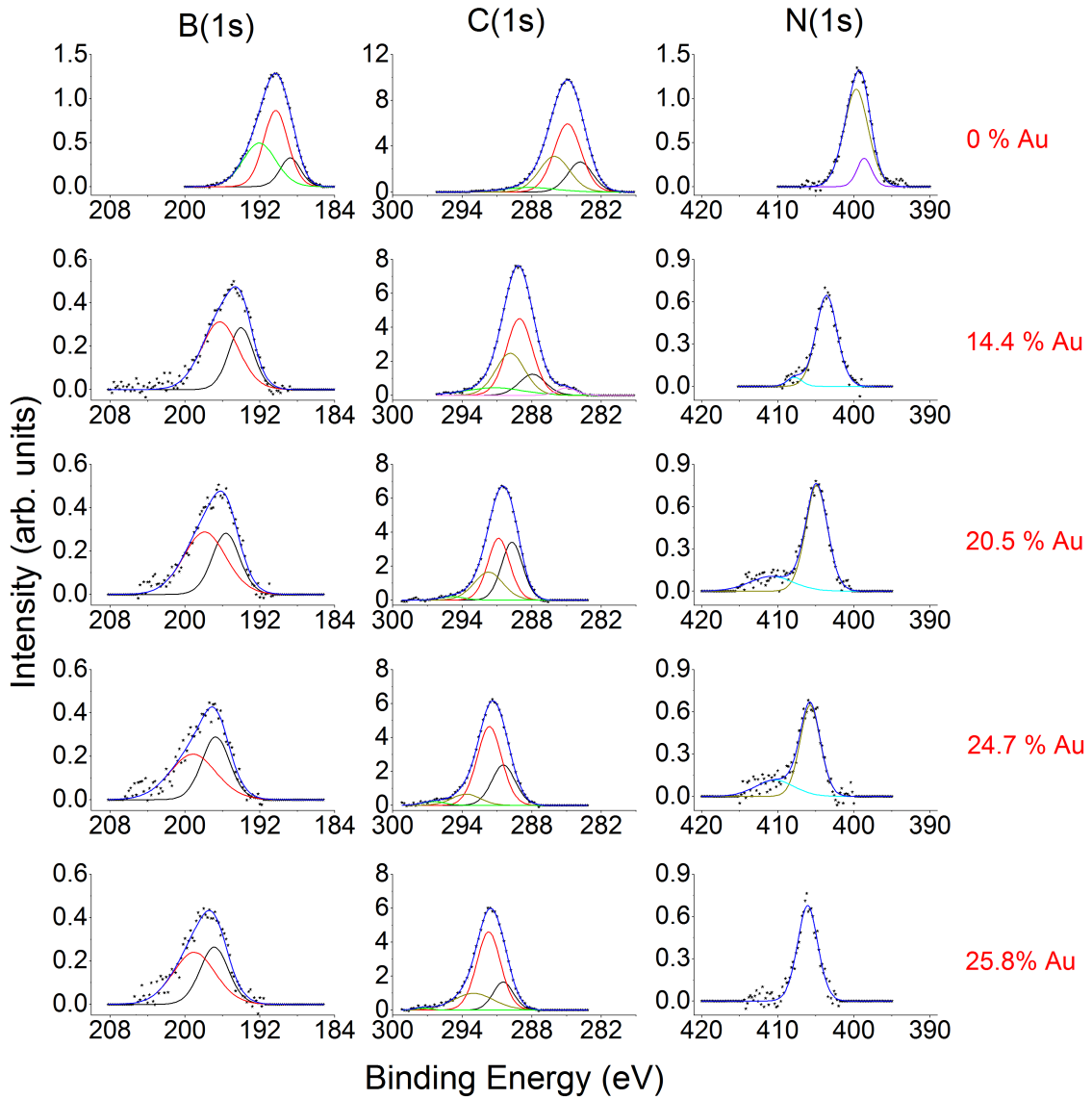


Figure 3.12: Evolution of the deconvoluted core level spectra of the B(1s) (left), C(1s) (middle) and N(1s) (right) as a function of the Au deposition for the boron carbide with aniline (*o*-BC:aniline) film.

tion. B-B species look to be more stronger with Au deposition, which is in agreement with the increasing on the relative atomic concentration seen in boron (table 3.3).

After Ar⁺ Sputtering

To determine the reversibility of Au surface interactions, both samples were Ar⁺ sputtered. Cycle times were varied from 15 min to 1h, and XPS spectra were acquired after each sputtering process. The results presented in this work, are related to the last sputtering process, and compared to the results from the cleaned sample, and to the results obtained after the last Au deposition on each sample.

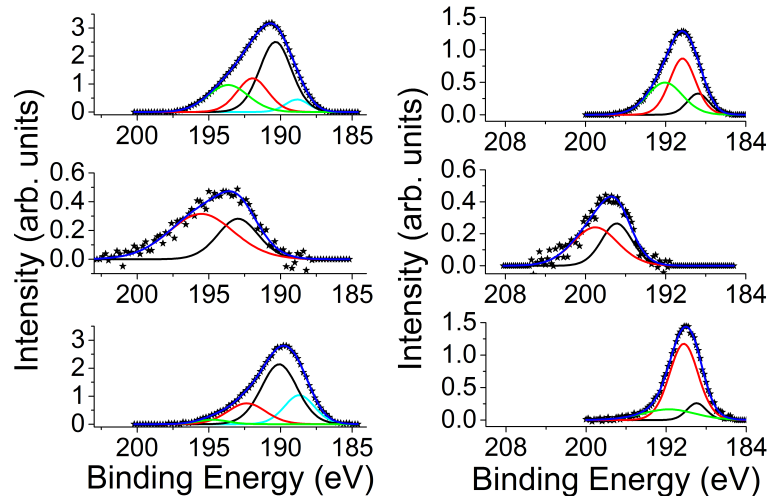


Figure 3.13: XPS core level spectra of the B (1s) when the sample was cleaned (top), after last Au deposition (middle), and after last Ar⁺ sputtering (bottom). Left: Pure *o*-BC, Right: *o*-BC:aniline.

Figure 3.13 shows the B(1s) core level for the three stages mentioned before, in the case of a) *o*-BC and b) *o*-BC:aniline. As it can be seen, the primary B(1s) peak is back to the original position, for both films, and it can be deconvoluted into the same main bonding environments (four in the case of *o*-BC, and three for the *o*-BC:aniline film). However, oxygen was removed easily, leading to weak oxide components, and more strong signal from other bonding environments present in each sample compared to the cleaned sample.

Although it is not shown in this graph, the Au feature present in the C(1s) core level spectra

for the case of the pure sample, and the one present in the N(1s) spectra for the sample containing aniline vanishes once the Au is cleaned. This is one more confirmation that there is not Au diffusion into the sample.

Table 3.5 summarizes the binding energies for each element in the sample before Au deposition, after the last Au deposition, and after cleaning the deposited Au. From this data, it is possible to deduce that the band bending at the surface due to the metal/semiconductor interface causes binding energies to shift to higher binding energies. And this effect is vanished, once the metal/semiconductor interface is removed, as expected.

Film	Stage	B(1s) eV	C(1s) eV	O(1s) eV	N(1s) eV
<i>o</i> -BC	Clean	190.8	285.1	533.8	–
	Final Au Dep.	193.0	288.2	535.7	–
	Final sputt.	189.7	284.1	532.8	–
<i>o</i> -BC:aniline	Clean	190.3	284.9	532.9	399.3
	Final Au Dep.	198.1	291.7	539.4	406.2
	Final sputt.	190.0	284.6	532.4	398.8

Table 3.5: XPS measured binding energies for the B(1s), C(1s), and N(1s) core levels for the pure boron carbide (*o*-BC) film and the pure boron carbide and aniline (*o*-BC:aniline) film at three different stages: before Au deposition, after the last Au deposition, and after cleaning the deposited Au.

***meta*-carborane based Samples**

As was mentioned in section 3.3, samples made from *meta*-carborane precursors form a n-type semiconductor. Thus, it is expected to find Schottky barrier formation when depositing Au on these type of films. Therefore, similar study as the one for p-type boron carbide semiconductor was carried out for pure *meta*-carborane boron carbide (*m*-BC) in

order to characterize the metal/semiconductor interface.

Figure 3.14 shows the evolution of B(1s), and C(1s) spectra with deposition and subsequent removal of an Au overlayer. The B(1s) spectra can be deconvoluted into two main peaks, one at low binding energy (188.3 eV) that corresponds to B-B species, and the second one at a higher binding energy (189.2 eV) which corresponds to B-C bonding environments. Sample was cleaned previous to the Au deposition. Although some oxygen was observed before sample cleaning, its intensity decreased after Ar^+ bombardment and no signal of boron oxides is seen in the B(1s) spectra.

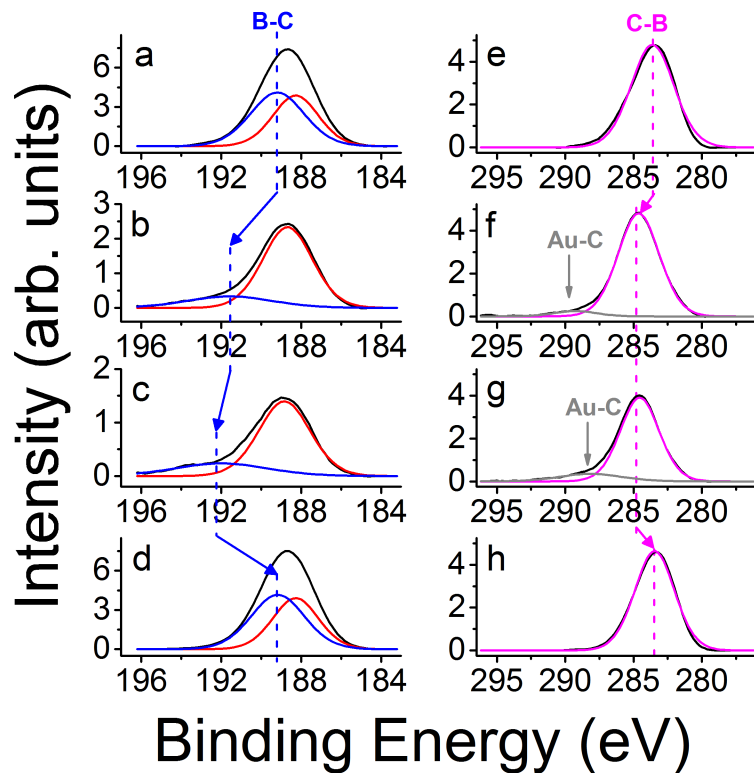


Figure 3.14: Evolution of the deconvoluted core level spectra of the B(1s) (left), and C(1s) (right) as a function of the Au deposition for the pure boron carbide (*m*-BC) film. a) and e) refer to the sample after cleaning, b) and f) refer to the first Au deposition, c) and g) refer to the last Au deposition, and d) and h) after Ar^+ sputtering.

	B(1s)		C(1s)	
	B-B Bond (eV)	B-C bond (eV)	C-B bond (eV)	C-Au bond (eV)
Clean sample	188.3	189.2	283.6	–
1rs Au deposition	188.7	191.5	284.6	289.3
2nd Au deposition	188.8	191.9	284.8	288.7
3rd Au deposition	188.8	192.1	284.8	288.3
1rs sputtering (15 min)	188.7	191.0	283.3	285.1
2nd sputtering (30 min)	188.6	189.8	283.4	–
3rd sputtering (30 min)	188.4	189.3	283.4	–
4th sputtering (1 h)	188.3	189.2	283.5	–

Table 3.6: XPS measured binding energies for the B(1s), and C(1s) core levels components as a function of the addition (deposition) and removal (Ar^+ bombardment or sputtering) of an Au overlayer.

As Au is deposited on the film, the peak representing B-C bonding environments moves to high binding energies, at the same time that its intensity decreases. However, it recovers its initial position and increases its intensity as Au is removed from the sample. In consequence, no Au diffusion occurs during the metal deposition. On other hand, the C(1s) core level spectra is deconvoluted into only one peak, corresponding to C-B bonding environments. As the samples is made from *meta*-carborane precursors no C-C bonds are expected as shown in Fig. 2.1b. No carbon oxides are clearly seen.

The C(1s) XPS spectra show a gradual increase in C(1s) binding energy and the addition of a satellite feature near 289 eV binding energy that appears with Au deposition and vanishes with the Au removal. This behavior is similar to the pure *o*-BC film. Thus, this feature is assigned to Au-C interactions. Table 3.6 summarizes the binding energies for all the derived boron and carbon components.

The increasing in core level binding energy of the C(1s) is significantly larger than the

observed for the B(1s) spectra, indicating that this effect cannot be ascribed to simple Au-induced band bending. However, compared to the values reported for the *ortho*-carborane based samples, these values are way smaller. Figure 3.15 shows the evolution of the B(1s) core level binding energy as the Au is deposited (black stars ★) and then removed (red triangles ◀).

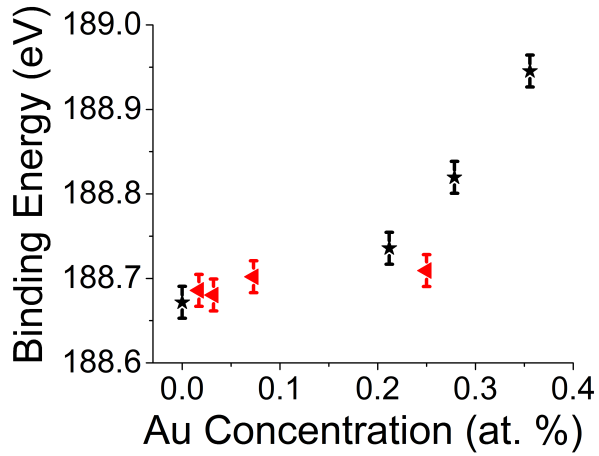


Figure 3.15: Shift in the binding energy of the B(1s) peak with increasing Au overlayer thickness deposition (black stars ★), and after Ar^+ bombardment to remove the gold overlayer (red triangles ◀).

If now a *meta*-carborane-base sample containing pyridine is studied, a similar effect as before is seen. The inclusion of pyridine is reflected in a bigger change in binding energy, but still small compared to the case of *ortho*-carborane samples. Figure 3.16 shows the binding energy shifts for B(1s) and C(1s) core level in both samples, pure *m*-BC and *m*-BC:Py.

While such a small increase in binding energy has been seen with the addition of a copper overlayer on various boron carbides[6-9], there are some subtle differences. Metacarborane (closo-1,7-dicarbadodecaborane) is unusual in that it is generally regarded as a n-type material [15-17,22]. As Au has a large work function (in the range of 5.3 eV to 5.5 eV

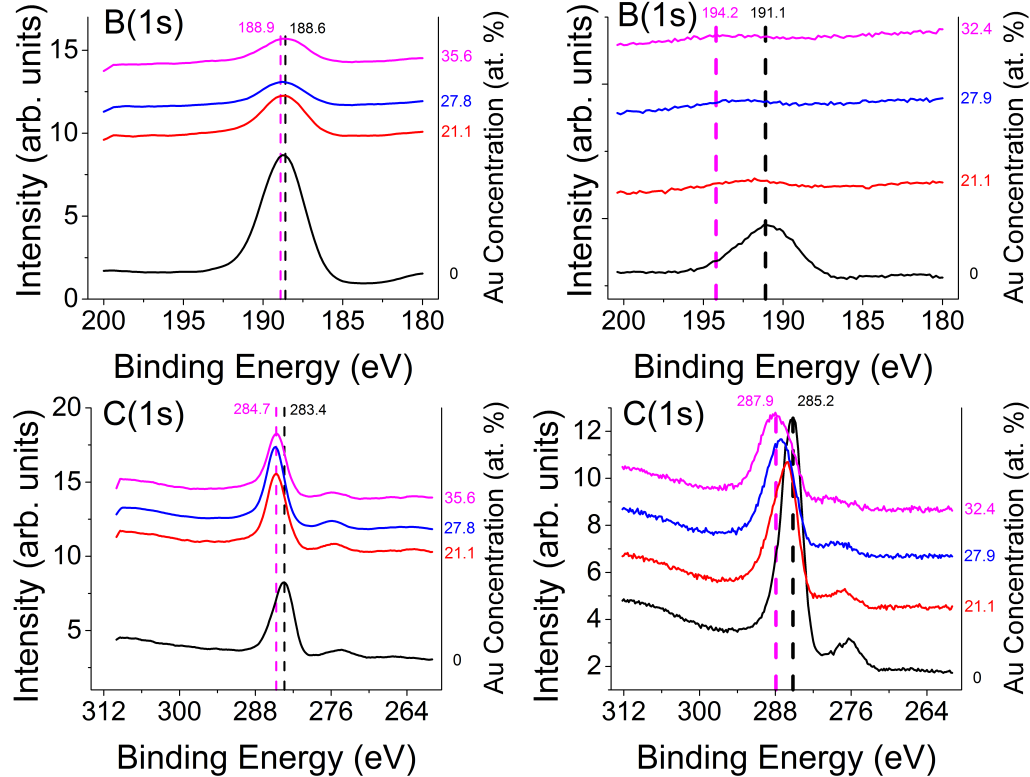


Figure 3.16: XPS core level spectra of the B(1s) (Top), and C(1s) (bottom) as a function of the Au deposition for *meta*-boron carbide-based samples. Left: Pure boron carbide (*m*-BC), Right: Boron carbide with pyridine (*m*-BC:Py)

[23-25]), this means that Schottky barrier formation should be favored as it is for many semiconductors (as mentioned before), and the apparent binding energy should decrease with increasing gold coverage.

The absence of the typical signatures of Schottky barrier formation, yet the strong interactions evident in the core level shifts and addition of a core level satellite features suggests that at least some extrinsic interface doping of the boron carbide by Au or formation of a metal-induced gap state at the interface. The facile manner in which gold can be removed from this boron carbide surface does suggest that diffusion of Au into the semiconductor surface region does not occur at room temperature.

The results shown in this thesis indicate that boron carbide seems to behave differently from other semiconductors, opening a way for new opportunities and approaches. Although different films were used here, other metals can be used to test these results. For example platinum (Pt) (with a work function in the range of 5.6 to 5.9 eV [25,26]), would be expected, according to the results presented in this thesis, to form a ohmic contact when depositing on a n-type boron carbide based films, and perhaps p-type boron carbide can be studied as well.

References

- [1] Echeverria, E., Dong, B., Liu, A., Wilson, E.R., Peterson, G., Nastasi, M., Dowben, P.A., Kelber, J.A. Strong binding at the gold (Au) boron carbide interface. *Surf. Coat. Technol.* **314** (2017) 51-54
- [2] 77th Physical Electronics Conference.
- [3] Pierret, R.F. *Semiconductor Device Fundamentals*. 2nd edition (1996) (Reading, MA: Addison-Wesley)
- [4] Neudeck, G.W. *The PN Junction Diode*. Vol II, 2nd edition (1989) (Reading, MA: Addison-Wesley)
- [5] Streetman, B.G. *Solid State Electronic Devices*. 4th edition (1995) (Englewood, NJ: Prentice Hall)
- [6] Driver, M.S., Paquette, M.M., Karki, S., Nordell, B.J., Caruso, A.N. The electronic and chemical structure of the a- $B_3CO_{0.5}$: H_y -to-metal interface from photoemission spectroscopy: implications for Schottky barrier heights. *J. Phys. Condens. Matter* **24** (2012) 445001
- [7] King, S.W., French, M., Xu, G., French, B., Jaehnig, M., Bielefeld, J., Brockman, J., Kuhn, M. Valence band offset and Schottky barrier at amorphous boron and boron carbide interfaces with silicon and copper. *Appl. Surf. Sci.* **285P** (2013) 545

- [8] King, S.W., French, M., Bielefeld, J., Jaehnig, M., Kuhn, M., French, B. X-ray photo-electron spectroscopy investigation of the Schottky barrier at a-BN:H/Cu interfaces. *Electrochim. Solid-State Lett.* **14** (2011) H478
- [9] James, R., Pasquale, F.L., Kelber, J.A. Plasma-enhanced chemical vapor deposition of ortho-carborane: structural insights and interaction with Cu overlayers. *J. Phys. Condens. Matter* **25** (2013) 355004
- [10] Hwang, S., Yang, K., Dowben P.A., Ahmad, A.A., Ianno, N.J., Li, J.Z., Lin, J.Y., Jiang, H.X., McIlroy, D.N. Fabrication of n-type nickel doped $B_5C_{1+\delta}$ homojunction and heterojunction diodes. *Appl. Phys. Lett.* **70** (1997) 1028
- [11] Hwang, S., Remmes, N.B., Dowben, P.A., McIlroy, D.N. Nickel doping of boron carbide grown by plasma enhanced chemical vapor deposition. *J. Vac. Sci. Technol., B* **14** (1996) 2957
- [12] Hwang, S., Remmes, N., Dowben, P.A., McIlroy, D.N. Nickel doping of boron carbide and corresponding Fermi level shifts. *J. Vac. Sci. Technol. B* **15** (1997) 854
- [13] Carlson, L., Lagraffe, D., Balaz, S., Ignatove, A., Losovyj, Y.B., Choi, J., Dowben, P.A., Brand, J.I. Doping of boron carbides with cobalt, using cobaltocene. *Appl. Phys. A Mater. Sci. Process.* **89** (2007) 195
- [14] Lunca-Popa, P., Brand, J.I., Balaz, S., Rosa, L.G., Boag, N.M., Bai, M., Robertson, B.W., and Dowben, P.A. Evidence for multiple polytypes of semiconducting boron carbide (C_2B_{10}) from electronic structure. *J. Phys. D: Appl. Phys.* **38** (2005) 1248-1252

- [15] Peterson, G., Su, Q., Wang, Y., Dowben, P., Nastasi, M. Improved p-n heterojunction device performance induced by irradiation in amorphous boron carbide films. Mater. Sci. Eng. B 202 (2015) 25
- [16] B.W. Robertson, S. Adenwalla, A. Harken, P. Welsch, J.I. Brand, P.A. Dowben, J.P. Claassen, A class of boron-rich solid-state neutron detectors, Appl. Phys. Lett. 80 (2002) 3644.
- [17] Caruso, A.N., Balaz, S., Xu, B., Dowben, P.A., McMullen-Gunn, A.S., Brand, J.I., Losovyj, Y.B., McIlroy, D.N. Surface photovoltage effects on the isomeric semiconductors of boron-carbide. Appl. Phys. Lett. 84 (2004) 1302
- [18] Kolel-Veetil, M.K., Gamache, R.M., Bernstein, N., Goswami, R., Qadri, S.B., Fears, K.P., Miller, J.B., Glaser, E.R., Keller, T.M. Substitution of silicon within the rhombohedral boron carbide (B_4C) crystal lattice through high-energy ball-milling. J. Mater. Chem. C 3 (2015) 11705
- [19] Pasquale, F.L., Liu, J., Dowben, P.A., Kelber, J.A. Novel semiconducting alloy polymers formed from ortho-carborane and 1,4-diaminobenzene. Mater. Chem. Phys. 133 (2012) 901
- [20] Mthethwa, T., Antunes, E. and Nyokong, T. Photophysical properties of a new water soluble tetra thiamine substituted zinc phthalocyanine conjugated to gold nanorods of different aspect ratios. Dalton Trans., 43 (2014) 8230
- [21] Losito, I., De Giglio, E., Cioffi, N. and Malitesta, C. Spectroscopic investigation on polymer films obtained by oxidation of *ortho*-phenylenediamine on platinum electrodes at different pHs. J. Mater. Chem. 11 (2001) 1812-1817

- [22] Osberg, K., Schemm, N., Balkir, S., Brand, J.I., Hallbeck, M.S., Dowben, P.A., Hoffman, M.W. A handheld neutron-detection sensor system utilizing a new class of boron carbide diode, *IEEE Sensors J.* **6** (2006) 1531-1538
- [23] W.M.H. Sachtler, G.J.H. Dorgelo, A.A. Holscher, The work function of gold, *Surf. Sci.* **5** (1966) 221.
- [24] H.C. Potter, J.M. Blakeley, LEED, Auger spectroscopy, and contact potential studies of copper-gold alloy single-crystal surfaces, *J. Vac. Sci. Technol.* **12** (1975) 635.
- [25] P.E.C. Franken, V. Ponec, Ethylene adsorption on thin films of Ni, Pd, Pt, Cu, Au and Al; work function measurements, *Surf. Sci.* **53** (1975) 341.
- [26] B.E. Nieuwenhuys, W.H.M. Sachtler, Crystal face specificity of nitrogen adsorption on a platinum field emission tip, *Surf. Sci.* **34** (1973) 317.

Chapter 4

PYRIDINE

Introduction

In this chapter the effects of incorporating the aromatic compound pyridine (C_5H_5N) in carborane-derived boron carbide films will be discussed. All the samples investigated were grown by PECVD on clean n-type Si, and synthesized from *ortho*-carborane. Pure boron carbide samples will be identified as *o*-BC, while films with carborane/pyridine ratios of 1:x will be labeled as *o*-BCPy(1:x), with x indicating the pyridine content.

The results presented in this chapter were published in [1-3], coauthor with George Petersen and others.

Samples Composition

As it was mentioned in section 2.2.2, different ratios of carborane/pyridine can be obtained by varying the flow rate of the pyridine while keeping constant the flow rate of the ortho-carborane. During the growth process, XPS measurements were carried out in order to characterize the film deposition. The binding energies peaks for the *o*-BCPy(1:x) samples

do not vary significantly through the deposition process.

The pyridine/orthocarborane ratios of the various films were determined by XPS from the analysis of the core level intensities corrected for cross-section and analyzer transmission function using standard methods [4,5]. These allowed derivation of the relative atomic composition ratios B/N and B/C. Experimental and calculated values are shown in Table 4.1. And it is clear that the very good agreement between both ratios demonstrates that the films contain negligible N or C contamination from external sources.

Films	Experimental atomic ratio		Calculated atomic ratio	
	B/N	B/C	B/N	B/C
<i>o</i> -BCPy(1:2)	4.76	0.75	5.00	0.83
<i>o</i> -BCPy(1:3)	3.57	0.62	3.33	0.61
<i>o</i> -BCPy(1:5)	1.82	0.34	2.00	0.34
<i>o</i> -BCPy(1:7)	1.43	0.26	1.43	0.26
<i>o</i> -BCPy(1:10)	1.05	0.21	1.00	0.21

Table 4.1: Experimental B/N and B/C atomic ratios, and corresponding pyridine/orthocarborane ratios with calculated B/N and B/C atomic ratios assuming intact precursors in deposited films.

The estimation of the B/N and B/C atomic ratios and corresponding pyridine/orthocarborane ratios were made on the assumption that both the carborane and pyridine moieties remain essentially intact under these plasma deposition conditions. This statement has been previously demonstrated in [6,7].

For this study, three types of boron carbides thin films are discussed: (i) pure boron carbide films, *o*-BC, (ii) boron carbide films with a pyridine concentration roughly proportional to the icosahedral carborane moieties, *o*-BCPy(1:3), (iii) boron carbide films with a relatively high pyridine concentration relative to the icosahedral carborane (BC) moieties,

o-BCPy(1:10).

Spectroscopic ellipsometry

The band gap of the samples was determined from the imaginary part of the dielectric function as discussed in section 2.4.0.1. The real (a) and imaginary (b) part of the modeled dielectric function is shown in 4.1, with vertical arrows indicating the band gap values for *o*-BC and *o*-BCPy(1:3) films¹.

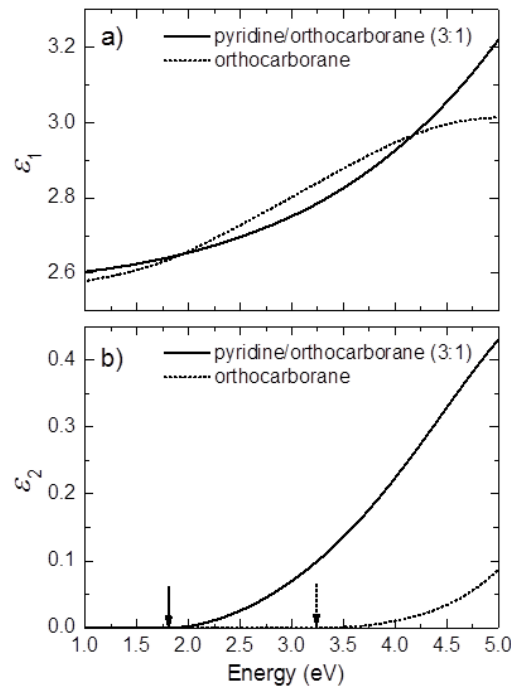


Figure 4.1: Dielectric function spectra for *o*-BC (dotted line) and *o*-BCPy(1:3) (solid line) films. a) Real part (ϵ_1) b) Imaginary part (ϵ_2). Vertical arrows indicate the band gap energy determined using the Tauc-Lorentz model described in section 2.4.0.1.

Calculated values for the thickness and band gap of the samples, based on VASE, are summarized in table 4.2. The thickness values, determined by VASE, are in qualitative

¹ From equation 2.3 we know that the imaginary part of the dielectric is zero if $E \leq E_g$, and different to zero otherwise, therefore the band gap values can be easily identified.

agreement with those estimated from extrapolation of XPS-derived growth rates during PECVD. The increase in film thickness is a partial compensation for the decrease in the boron density as the pyridine moieties increase in concentration.

Films	Thickness (nm) by XPS	Thickness (nm) by VASE	Band Gap, E_g , (eV)
<i>o</i> -BC	~ 165	483	3.2 ± 0.1
<i>o</i> -BCPy(1:3)	~ 350	557	1.8 ± 0.1
<i>o</i> -BCPy(1:10)	~ 720	480	1.6 ± 0.1

Table 4.2: Calculated thickness and band gaps of the studied films.

While the band gap of the films decreases with pyridine inclusion, the band gap seems to saturate at with modestly high pyridine content, decreasing no further. These results are in agreement with trends observed in the density functional theory (DFT) calculations. For carboranes linked by linear chains of pyridine, the calculated orbital binding energies of the highest occupied molecular orbital (HOMO) and the lowest unoccupied molecular orbital (LUMO) are plotted as a function of pyridine number in Fig. 4.2 [1]. A reduction on the band gap is observed from 6.6 eV for pure molecular precursors to 2.7 eV for partly hydrogenated semiconducting boron carbide samples with high pyridine concentration.

Although it is not shown in this dissertation, optical measurements on samples containing aniline showed a similar behavior: aniline inclusion decreases the band gap of the pure boron carbide from 3.2 eV to 1.3 eV for high concentrations of the aromatic moieties [8].

Ultraviolet photoelectron spectroscopy (UPS) measurements were carried out also to investigate the position of valence band of the films. The results show that the valence band maximum (VBM) of the films shifts to a lower binding energy with pyridine inclusion, as

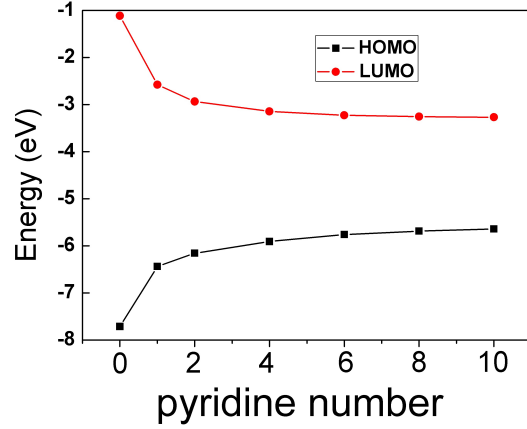


Figure 4.2: Band gap energy as a function of pyridine inclusion, from density functional theory (DFT) calculations, carried out by the group of Wai-Ning Mei.

seen in Fig. 4.3, indicating an increasing in the p-type behavior of the samples.

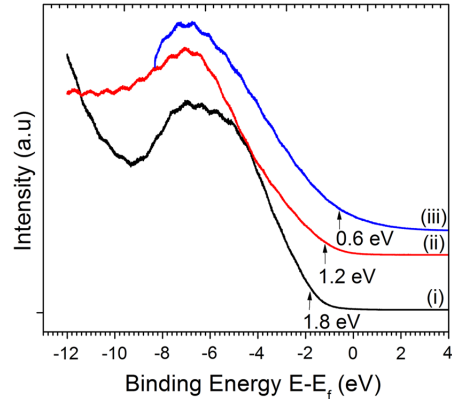


Figure 4.3: Comparison of the UPS spectra of the valence bands of (i) *o*-BC (black line), (ii) *o*-BCPy(1:7) (red line), and (iii) *o*-BCPy(1:22) (blue line). Black arrows/number mark the positions/energies of the various valence band maxima below the Fermi level ($E_F = 0$). All films are on clean Si. Peak maxima are set at 7 eV.

A peak at about - 7 eV is clearly seen in all the spectra. This peak is characteristic of the pure *o*-BC, while the shift in the binding energy of the VBM reflects that the extra density of states at lower binding energies are due to the states exclusively present in the pyridine [9,10], and suggest an increasing p-type behavior on the samples containing pyridine moieties.

Device Heterostructures

All three films used in this study are p-type. The increasingly p-type behavior suggested by the decreasing binding energy of the VBM in the photoemission spectra (Fig. 4.3) is consistent with the heterostructure diode behavior when deposited on n-type Si as shown in Fig. 4.4.

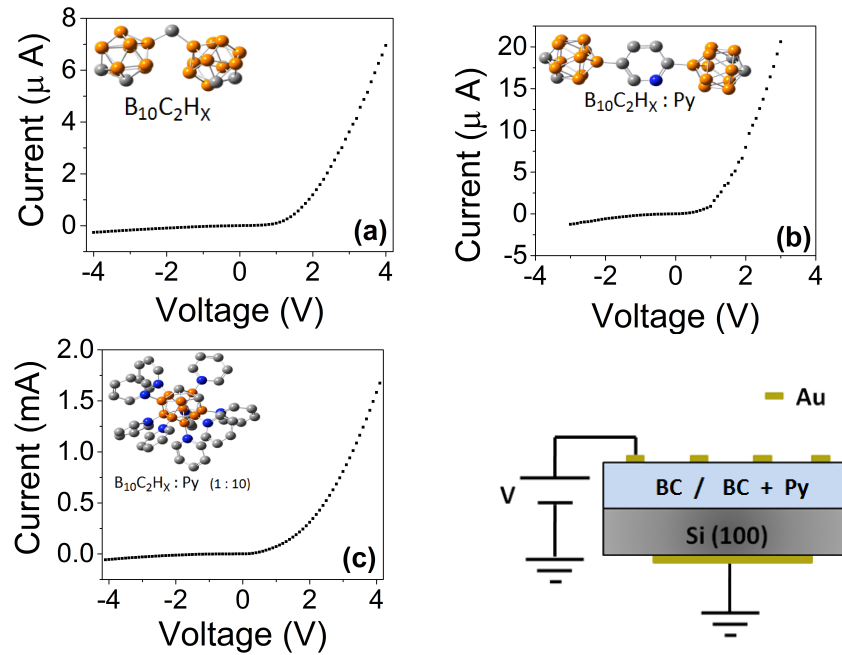


Figure 4.4: Heterojunction of boron carbides on silicon where the boron carbide was fabricated (see section 2.2) from a) *ortho*-carborane (*o*-BC), b) *ortho*-carborane plus pyridine in the ratio 1:1 (*o*-BCPy(1:1)), and c) *ortho*-carborane plus pyridine in the ratio 1:10 (*o*-BCPy(1:10)). A schematic picture of the diode structure is also shown.

All films show the expected rectification of prior similar devices [11-20]. The inclusion of pyridine with the icosahedral building blocks of boron carbide film does not seem to significantly alter or increase the normalized reverse bias leakage current (Fig. 4.5); if anything, the boron carbide formed with high concentration of pyridine may provide marginally better rectification. This is desirable.

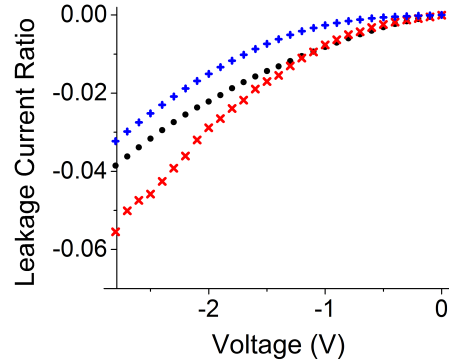


Figure 4.5: Reverse bias current normalized to the 3 V forward bias current. ($\bullet\bullet$ *o*-BC, $\times\times$ *o*-BCPy(1:1), and $+\!+$ *o*-BCPy(1:10) films.

The C(V) curves for samples containing Py (*o*-BCPy) show no frequency-dependence at reverse bias, as seen in Fig. 4.6b, even though pure boron carbide samples (*o*-BC) show a significant frequency dependence (Fig. 4.6a). The capacitance does decrease with increasing frequency, however, indicating that there is some type of charge carrier that can no longer respond to the perturbation signal as the frequency increases [21-23].

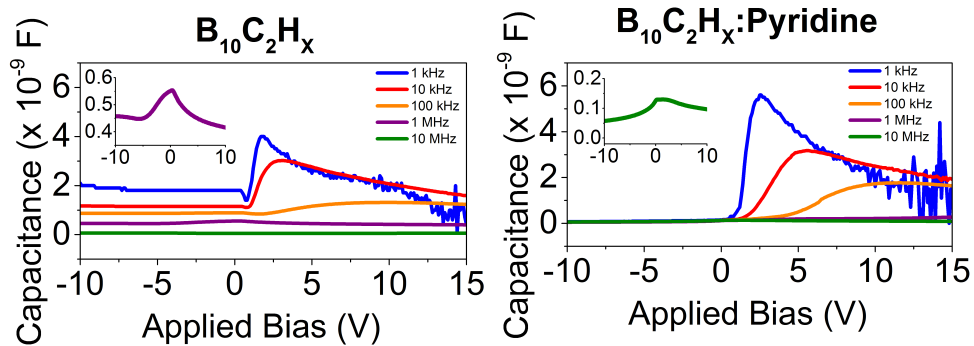


Figure 4.6: C(V) curves for the heterojunctions as a function of the frequency. The insets are of high frequency data on an expanded capacitance scale. Left: *o*-BC, Right: *o*-BCPy

The peak capacitance values of the *o*-BCPy diodes are slightly larger than those of *o*-BC films on silicon. There is also a shift of the peak capacitance toward positive bias in the *o*-

BCPy diodes, which is attributed to a decrease in the series resistance (R_S) of the *o*-BCPy. With the higher R_S , exhibited by the *o*-BC film, there is an associated voltage drop across the junction (equation 4.1), which will reduce the applied voltage shifting the signal toward zero, as observed.

$$V_J = V_A - IR_S \quad (4.1)$$

V_J is the junction voltage, V_A is the applied voltage, I is the current, and R_S .

From the I(V) and C(V) measurements it is possible to obtain the hole carrier lifetimes of the samples [1]. In this approach it is assumed that, under forward bias conditions, the contribution to the device capacitance is due to the diode diffusion capacitance (C_D). This capacitance is given by the equation:

$$C_D = \frac{G_0}{\omega \sqrt{s}} \left(\sqrt{1 + \omega^2 \tau^2} - 1 \right)^{\frac{1}{2}} \quad (4.2)$$

where G_0 is the low frequency conductance, which can be obtained from the slope of the I(V) curve ($G_0 = \frac{dI}{dV_A}$), $\omega = 2\pi f$ is the angular frequency, and τ is the effective carrier lifetime. Therefore, by modeling the diode diffusion capacitance (C_D) and comparing with the C(V) data for each sample, George Peterson showed it was possible to obtain the lifetime of the films [1].

The modeled C_D values have been fitted onto the measured C(V) data for 10 kHz, for both films: *o*-BC and *o*-BCPy. The agreement between our model and the data is very good for both diodes, as seen in Fig. 4.7.

The fitting of the equation 4.2 to the measured C(V) data in Fig. 4.6, taken at 10 kHz, for

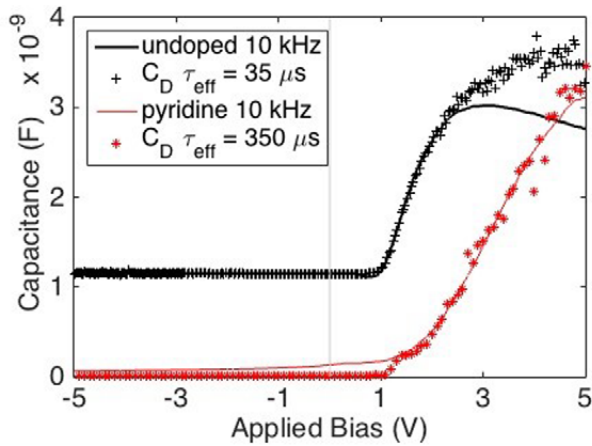


Figure 4.7: Model of diffusion capacitance overlaid on C(V) data at 10 kHz: undoped data (solid black line) and pyridine doped data (solid red line). The undoped calculated C_D (black +) indicates an effective carrier lifetime of $35 \mu s$. The pyridine doped calculated C_D (red *) indicates an effective carrier lifetime of $350 \mu s$. Modeling was carried out by George Peterson.

both diodes yields to values of the carrier lifetime of $350 \mu s$ for the *o*-BCPy heterojunction diode, and $35 \mu s$ for the *o*-BC diode. Thus, the inclusion of pyridine increases the lifetime of the films. One might expect that with the addition of pyridine-like moieties, there would be additional scattering centers, leading to a shorter lifetime. Just the opposite is observed. One possible explanation is the reduction in the trap concentration.

The *o*-BCPy film has only 1 frequency dependent capacitance component, the diffusion capacitance, while the *o*-BC heterojunction diode has two distinct frequency dependent capacitance components: the diffusion capacitance (common to both types of heterojunction diode), and the junction capacitance. The later component indicates that the *o*-BC films also have defect states that respond to the small signal perturbation. As the period of the perturbation approaches the lifetime of the carriers due to the defect state, the defects can no longer respond to the perturbation, and no longer contribute to the capacitance of the diode. Traps result in contributions to capacitor charging current, but since their time constants are relatively long, the effects of the traps are absent, or greatly reduced, with high

frequency perturbations.

This indicates that the addition of pyridine to the PECVD semiconducting hydrogenated boron carbide is eliminating key trap states within the device, therefore the lifetime of the films is increased. But, not only aromatic compounds inclusion has shown to increase the drift carrier lifetime compared to the pure boron carbide, the use of *ortho*-carborane or *meta*-carborane has an effect on these carrier lifetimes [25]. Table 4.3 shows the hole carrier lifetimes of different samples.

SAMPLE	<i>o</i> -carborane based	<i>m</i> -carborane based
Pure Boron Carbide	$\leq 35 \mu s$	$50 ns$
Boron Carbide plus Pyridine	$350 \mu s$	Not measured yet
Boron Carbide plus Benzene	$2.5 ms$	$300 ns$

Table 4.3: Hole carrier lifetimes of the studied films.

C(V) measurements on samples containing benzene showed no frequency dependence at reverse bias, which is in accordance with the results showed for BC:Py films.

Neutron Capture

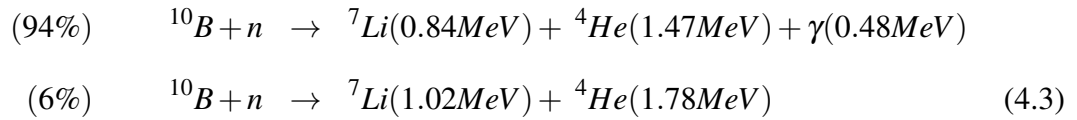
Neutron detection plays an important role in different areas ranging from nuclear science [26,27], medicine [28-30], and homeland security applications [32-34]. Neutrons are characterized by their lack of charge, and their low interaction with matter, which make their direct detection difficult and challenging.

Currently, one of the processes used to detect neutrons is through nuclear reactions (used for slow or thermal neutrons) where they are captured. Both 3He and ^{10}B (as well as 6Li ,

and ^{157}Gd , etc.) are suitable targets. To solve the ^3He supply problem [31], we need solid state detectors, which is the point of investigating a semiconductor boron carbide.

These nuclear reactions create charged particles more easily detected by radiation detectors, since they can produce ionization on the material, and then an electrical signal which can be easily measured. Therefore, elements with high capture cross section are desirable for building the detector. However, there are really few elements with this characteristic that, additionally, can be made into solid state semiconductor neutron detectors.

Boron (specifically ^{10}B as ^{11}B has negligible neutron cross-section) has shown to be suitable, and indeed semiconducting devices based on boron carbide films have attracted considerable attention for neutron detection [11-15,24]. What makes the boron-rich icosahedral based boron carbide [35], boron nitride and boron phosphide [36,37] materials advantageous is that ^{10}B neutron capture yields high energy ions that are easily detectable when heterojunction diodes based on boron carbide are used [11-20]. Additionally, these materials have the ability to heal radiation damage. The interaction of the thermal neutrons with ^{10}B is given by equation 4.3:



As we have shown so far, inclusion of the pyridine improves the electron-hole separation on the films. Therefore, it is expected to have a better neutron captures for those samples containing pyridine. Accordingly, in this section, we address the effects of incorporating pyridine in carborane-derived boron carbide films for neutron detection.

The neutron irradiation and detection experiments used a Thermo Scientific MP 320 neutron generator. All diodes were placed on a grounded electrostatic shield and connected to a charge-to-voltage preamplifier (CANBERRA Model 2004), which is simultaneously connected to a pulse counter (Canberra, Digital signal processor 9600). Experiments were carried out at the University of Nebraska - Lincoln.

The pulse height spectra at zero bias for *o*-BC and *o*-BCPy(1:10) are shown in Fig. 4.8². As expected, both devices exhibit a distinctly different spectrum. The film with heavy inclusion of pyridine (*o*-BCPy(1:10)) present a clearly separated peak, representative of much larger pulse heights and of significantly high intensity compared to the pure boron carbide. This signature in the pulse heights spectra clearly indicates the improved electron hole separation, and better charge collection of the electron-hole pairs generated after neutron capture.

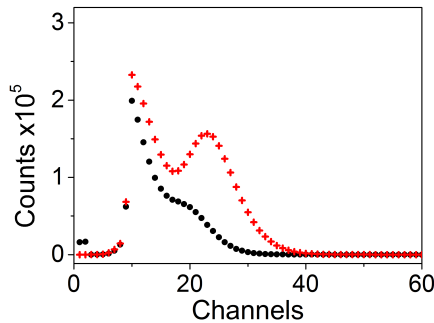


Figure 4.8: The experimental neutron pulse height spectra at ZERO applied bias. (●● *o*-BC, + + *o*-BCPy(1:10)).

Some incomplete charge collection is expected for solid state devices based on boron neutron capture generated electron-hole pair production, especially for very thin films at zero bias [20]. This means a lot of counts at the low channel (small pulse height) numbers.

² Channel number is proporcional to pulse energy.

These counts are difficult to distinguish from the device current. Smaller or zero bias decrease the dark current but also decreases the charge collection from charge creation. For very thin films of this semiconductor containing boron, the behavior seen here is similar to the charge collection or pulse height spectra observed at higher reverse bias for thin boron containing solid state neutron detectors [20]. This strongly indicates that the improvements in charge collection seen here, after neutron capture, are due to the materials modification. These results are a solid indication that improved charge collection at zero bias are possible without an increased reverse bias. There may even be some marginal improvements in the overall pulse collection.

These results are consistent with the longer carrier lifetimes found for *o*-BCPy films, confirming the improvement on the electron-hole separation and carrier lifetimes on the boron carbide heterojunctions due to pyridine inclusion.

References

- [1] Echeverria, E. et al., Semiconducting boron carbides with better charge extraction through the addition of pyridine moieties. *J Phys D Appl Phys* **49** (2016) 355302
- [2] Echeverria, E. et al., Novel semiconducting boron carbide/pyridine polymers for neutron detection at zero bias. *Appl. Phys. A*, Vol. **118** issue 1 (2014) 113-118.
- [3] Echeverria, E. et al., Neutron Detection Signatures at Zero Bias in Novel Semiconducting Boron Carbide/Pyridine Polymers, *Mater. Res. Soc. Symp. Proc.* **Vol.1** (2015)
- [4] M., Aronniemi, Sainio, J., and Lahtinen, J. Chemical state quantification of iron and chromium oxides using XPS: the effect of the background subtraction method. *Surf. Sci.* **578** (2005), p.108
- [5] P.M.A. Sherwood. Data analysis in XPS and AES, D. Briggs, M.P. Seah (Eds.), *Practical Surface Analysis*, vol. 1, Auger and X-ray Phototoelectron Spectroscopy (second ed.), John Wiley & Sons, Inc. (1990), p. 555
- [6] Dong, B., James, R. and Kelber, J.A. PECVD of boron carbide/aromatic composite films: Precursor stability and resonance stabilization energy. *Surf. Coat. Technol.* **290** (2016) 94-99

- [7] James, R., Pasquale, F.L. and Kelber, J.A. Plasma-enhanced chemical vapor deposition of ortho-carborane: structural insights and interaction with Cu overlayers. *J. Phys.:Condens. Matter* **25** (2013) 355004
- [8] Dong, B., Echeverria, E., Oyelade, A., Knight, S., Schubert, M., Dowben, P.A., and Kelber, J.A. Chemical and Electronic Structure of Aniline/Orthocarborane Composite Films. **Submitted**
- [9] Pasquale F.L., Li, Y., Du, J.C., Kelber, J.A. Novel alloy polymer formed from ortho-carborane and benzene or pyridine. *J. Phys.: Condens. Matter* **25** (2013) 105801. doi:10.1088/0953-8984/25/10/105801
- [10] Pasquale, F.L., James, R., Welch, R., Echeverria, E., Dowben, P.A., Kelber, J.A. Novel cross-linked ortho-carborane and ortho-carborane: Y (Y = 1,4-diaminobenzene, pyridine, benzene) polymer films: a new class of carborane-based materials with tunable electronic structure *ECS Trans.* **53** (2013) 303-310. doi:10.1149/05301.0303ecst
- [11] Caruso, A.N., The physics of solid-state neutron detector materials and geometries. *J. Phys.: Condens. Matter* **22** (2010) 1-32. doi:10.1088/0953-8984/22/44/443201
- [12] Caruso, A.N., Billa, R.B., Balaz, S., Brand, J.I., Dowben, P.A. The heteroisomeric diode. *J. Phys.: Condens. Matter* **16** (2004) L139-L146 (2004). doi:10.1088/0953-8984/16/10/L04
- [13] Robertson, B.W. et al., A Class of boron-rich solid-state neutron detectors. *Appl. Phys. Lett.* **80** (2002) 3644-3646. doi:10.1063/1.1477942
- [14] Robertson, B.W. et al., Semiconducting boron-rich neutron detectors. *Proc. SPIE* **4785** (2002) 226-233. doi:10.1117/12.453923

- [15] Adenwalla, S. et al., Semiconducting boron-rich neutron detectors. Proc. SPIE **5199** (2004) 70-74. doi:10.1117/12.
- [16] Osberg, K. et al., A Handheld Neutron-Detection Sensor System Utilizing a New Class of Boron Carbide Diode. IEEE Sens. J. **6** (2006) 1531-1538. doi:10.1109/JSEN.2006.883905
- [17] Osberg, K. et al., A hand-held neutron detection sensor system. IEEE Int. Symp. Circ. (2006) 1179-1182. doi:10.1109/ISCAS.2006.1692801
- [18] Caruso, A.N. et al., The all boron carbide diode neutron detector: Comparison with theory. Mater. Sci. Eng. **135** (2006) 129-133. doi:10.1016/j.mseb.2006.08.049
- [19] Day, E., Diaz, M.J., Adenwalla, S. Effect of bias on neutron detection in thin semiconducting boron carbide films. J. Phys. D Appl. Phys. **39** (2006) 2920-2924. doi:10.1088/0022-3727/39/14/007
- [20] Hong, N., Mullins, J., Foreman, K., Adenwalla, S. Boron carbide based solid state neutron detectors: the effects of bias and time constant on detection efficiency. J. Phys. D Appl. Phys. **43** (2010) 275101. doi:10.1088/0022-3727/43/27/275101
- [21] Nicollian E.H. and Goetzberger A. The Si-SiO₂ Interface - Electrical Properties as Determined by the Metal-Insulator-Silicon Conductance Technique. Bell Syst. Tech. J. **46** (1967) 1055
- [22] Nicollian E.H. and Brews J.R. MOS (Metal Oxide Semiconductor) Physics and Technology. 1982 New York, Wiley-Interscience, 1982. 920 p
- [23] Sze S.M. and Ng K.K. Physics of Semiconductor Devices, 2006 John Wiley & Sons, Inc.

- [24] Peterson, G., Su, Q., Wang, Y., Dowben, P., Nastasi, M. Improved p-n heterojunction device performance induced by irradiation in amorphous boron carbide films. *Mater. Sci. Eng. B* **202** (2015) 25
- [25] Peterson, G.G., Echeverria, E., Dong, B., Silva, J.P., Wilson, E.R., Kelber, J.A., Nastasi, M., Dowben, P.A. Increased drift carrier lifetime in semiconducting boron carbides deposited by plasma enhanced chemical vapor deposition from carboranes and benzene. *Journal of Vacuum Science & Technology A: Vacuum, Surfaces, and Films* **35** (2017) 03E101
- [26] R.S. Seymour, B. Richardson, M. Morichi, M. Bliss, R.A. Craig, D.S. Sunberg, Scintillating-Glass-Fiber Neutron Sensors, their Application and Performance for Plutonium Detection and Monitoring, *Journal of Radioanalytical and Nuclear Chemistry*, **243(2)** (2000) 387-388
- [27] Nuclear Regulatory Commission, Special Nuclear Material, accessed January, 2012. [Online]. Retrieved from <http://www.nrc.gov/materials/sp-nucmaterials.html>
- [28] C.W.E. van Eijk, Inorganic scintillators in medical imaging, *Phys. Med. Biol.* **47** (2002) R85-R106
- [29] E.J. Hall. Radiobiology for the Radiologist. Lippincott Williams & Wilkins; 5th edition, (2000)
- [30] H.E. Johns and J.R Cunningham. The Physics of Radiology. Charles C Thomas 3rd edition, (1978)
- [31] Kouzes R.T. 2009. The ^3He Supply Problem. PNNL-18388, Pacific Northwest National Laboratory, Richland, WA.

- [32] Kouzes R.T., Detecting Illicit Nuclear Materials. *American Scientist*, **93(5)** (2005) 422-427
- [33] Kouzes R.T. 2010 and Ely J.H., Status Summary of ^3He and Neutron Detection Alternatives for Homeland Security. PNNL-19360, Pacific Northwest National Laboratory, Richland, WA.
- [34] Van Ginhoven, R.M., R.T. Kouzes, and D.L. Stephens, Alternative Neutron Detector Technologies for Homeland Security. PNNL-18471, Pacific Northwest National Laboratory, Richland, WA.
- [35] Simeone, D., Mallet, C., Dubuisson, P., Baldinozzi, G., Gervais, C., Maquet, J. Study of boron carbide evolution under neutron irradiation by Raman spectroscopy. *J. Nuclear Materials* **277** (2000) 1-10. doi: 10.1016/S0022-3115(99)00149-X
- [36] Emin, D. Unusual properties of icosahedral boron-rich solids. *Journal of Solid State Chemistry* **179** (2006) 2791-2798. doi:10.1016/j.jssc.2006.01.014
- [37] Carrard, M., Emin, D., and Zuppiroli, L. Defect clustering and self-healing of electron-irradiated boron-rich solids. *Phys. Rev. B* **51** (1995) 11270-11274. doi:10.1103/PhysRevB.51.11270

Chapter 5

MAGNETO-RESISTANCE

Introduction

Although the ability to control the resistance of a material, with an applied magnetic field, has been studied for a long time, it is still an ongoing field of interest. Applications of this phenomenon include hard disk drives, spin valve sensors, magnetoresistive sensors, spintronics, and metal oxide semiconductor field-effect transistor, among others.

Semiconducting boron carbides tend to be both highly resistive [1-3] and very defective [4,5], so there may be considerable enhancements to be had in the magnetoresistance of a heterostructure containing some boron carbides. This work addresses whether large room temperature magnetoresistance effects are in fact possible in semiconducting boron carbides.

All samples studied in this section were formed by cross-linking [6-8] of the icosahedral closo-1,2-dicarbadodecaborane (*ortho*-carborane; 1,2- $B_{10}C_2H_{12}$) in the presence of 1,4-diaminobenzene (BC:DAB films), or by cross-linking *ortho*-carborane without DAB additions (BC films).

Photoemission Spectroscopy

Figure 5.1 shows the B(1s), C(1s), O(1s) and N(1s) core levels for the cross-linked BC:DAB film. The measured X-ray photoemission binding energies are 189.7 eV, 285.3 eV, 532.5 eV and 400.2 eV for the B(1s), C(1s), O(1s) and N(1s) core levels, respectively. The B(1s) and C(1s) core level photoemission spectra are typical of those observed for $B_{10}C_2H_x$ films [6-12], condensed *ortho*-carborane multilayers [13], as well as the values obtained in section 3.3.1.1.

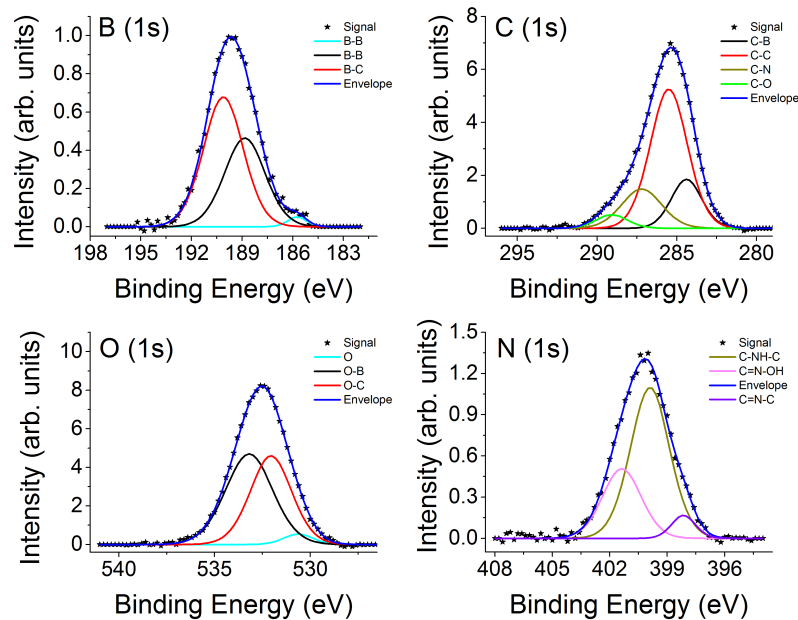


Figure 5.1: Core level spectrum of the B(1s), C(1s), O(1s) and N(1s) core levels for cross-linking *ortho*-carborane with DAB additions (BC:DAB) films.

The B(1s) core level is deconvoluted into three main peaks, two of them representing bonding environments due to B-B species (at 185.7 eV and 188.8 eV) and one (at 190.1 eV) representing B-C species [6-10,14]. No evidence of boron oxide is observed in the signal. The C(1s) core level photoemission spectrum (Fig. 5.1) is composed of four main peaks,

three of them characteristic of carbon atoms within the icosahedron and the carbon indicative of DAB ($C-B \rightarrow 284.4$ eV, $C-C \rightarrow 285.5$ eV, and $C-N \rightarrow 287.2$ eV) [7,8,21]. The peak at high binding energies, 289.0 eV, is characteristic of the carbon oxide.

The O(1s) core level is deconvoluted into three main peaks. The two peaks at high energy represent oxygen bonded to boron and oxygen bonded to carbon: $B-O \rightarrow 533.2$ eV, and $C-O \rightarrow 532.0$ eV. There is a small peak at 530.6 eV, similar to the case of the *o*-BC:Aniline film in section 3.3.1.1, therefore this peak is also associated to small oxygen contamination on the surface of the film.

The N(1s) core level photoemission spectra of the composite film exhibits a peak maximum identical to that of condensed DAB film [7,8]. The lack of significant perturbation of the N(1s) core level photoemission spectra from that of condensed DAB indicates that the N sites are not perturbed by the cross-linking process significantly. This signal can be deconvoluted into three different peaks: one at 401.3 eV representing C=N-OH species, one at 399.9 eV representing C-NH-C species, and finally one at 398.1 eV for C=N-C [16,21].

As was mentioned in section 2.2.2, samples growth by EBIC lead to more hydrogenate films compare to those growth by PECVD. The B(1s), C(1s) and N(1s) spectra do not change significantly, however, UPS spectra present different results depending on the used growth technique. The UPS spectra for films growth by EBIC with different aromatic compounds are compared in Fig. 5.2.

All of the UPS spectra present a maximum peak near to -9 eV, and are broader than those seen in Fig. 4.3 due to the high hydrogen content present in these samples. Hydrogen adds more density of states to the valence band, making the signal broader. The valence band

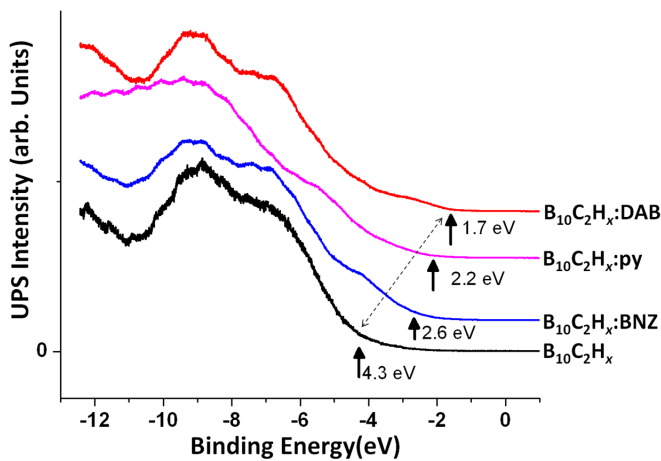


Figure 5.2: Comparison of the UPS spectra of the valence bands of hydrogenated boron carbide, hydrogenated boron carbide with benzene (BC:BNZ), hydrogenated boron carbide with (BC:Py) and hydrogenated boron carbide with diaminobenzene (BC:DAB). Data from ref. [7] and [19].

maximum, indicated by arrows in Fig. 5.2, also changes with the aromatic content making these samples more p-type compared to the pure boron carbide films. This is consistent with the shift seen in Fig. 4.3, therefore, this result is not an artificial effect of the technique used to grow the films, but a consequence of the addition of the aromatic compounds.

Magnetoresistance Measurements

Basic Principles

It is known that the resistance of a material can change with an applied magnetic field, this phenomenon is called magnetoresistance (MR). Depending on the type of the material, and the direction of the applied magnetic field, different types of magnetoresistance can be found. The most studied types are: ordinary, anisotropic, giant, geometrical, tunnel and colossal MR [18]. For the purpose of this work, only ordinary and giant MR will be considered.

Giant MR can appear when a non-magnetic material is placed in between of two thin layers of magnetic metals or ferromagnetic layers, as shown in Fig. 5.3. At zero magnetic field, the resistance of the sample has a given value, but when a magnetic field is applied, it increases or decreases significantly depending on the alignment of the magnetization of the metal/ferromagnetic material.

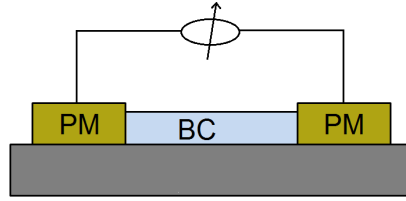


Figure 5.3: Schematic picture of the configuration to get giant magnetoresistance.

The MR can be defined by equation 5.3.1.

$$MR = \left(\frac{R(H)}{R(0)} - 1 \right) \times 100\% \quad (5.1)$$

where $R(H)$ is the resistance at an H value of the applied magnetic field (for this study it was chose as the maximum applied magnetic field), and $R(0)$ is the resistance at zero applied field [17].

The change in MR is due to the fact that electrons are scattered differently, depending on their spin orientation. This effect is known as spin dependent scattering [18].

Negative Magnetoresistance

In previous chapters, the I(V) curves on the semiconductor devices have been taken perpendicular to the surface of the film, i.e., contacts were placed on top (boron carbide side)

and bottom (silicon side) of the films, a voltage is applied across the film and the current is measured. Now, for the coming discussion, the contacts-voltage configuration will be as shown in Fig. 5.3.

The resistance as a function of the applied magnetic field was measured for the BC:DAB film at room temperature. Two different values of applied voltage were studied, 15 V and 20 V. By means of equation 5.3.1, the MR was obtained and plotted in Fig. 5.4. In both cases, the resistance of the film decreases as the magnetic field increases, therefore, the MR of the samples is negative, as seen in Fig. 5.4. Values of the resistance were of the order of $10^{10} - 10^{11} \Omega$. This is not new, as high resistivities are also characteristic of the PECVD semiconducting boron carbides [3] where a resistance of $10^{10} \Omega\text{-cm}$ is typical.

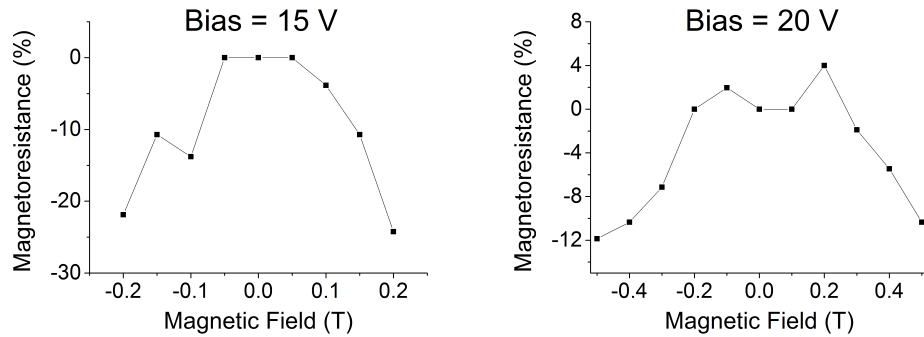


Figure 5.4: Magnetoresistance for a BC:DAB film at room temperature at a) 15 V bias, and b) 20 V bias. The distance between contacts is about 15 μm .

For a fixed bias voltage of 15 V at room temperature, the MR decreased by about 25%, while for a bias of 20 V it decreased about %12, both cases present values much larger than those reported in previous studies [1,2] undertaken at 77 K and 4.2 K. Samples were saturated easily, therefore, a second experiment was carried out to better analyze how the MR is affected by the applied voltage. In this experiment, instead of measuring directly the resistance of the sample as a function of the magnetic field, the I(V) curves were taken at

different values of applied magnetic field. Results for BC and BC:DAB samples are shown in Fig. 5.5.

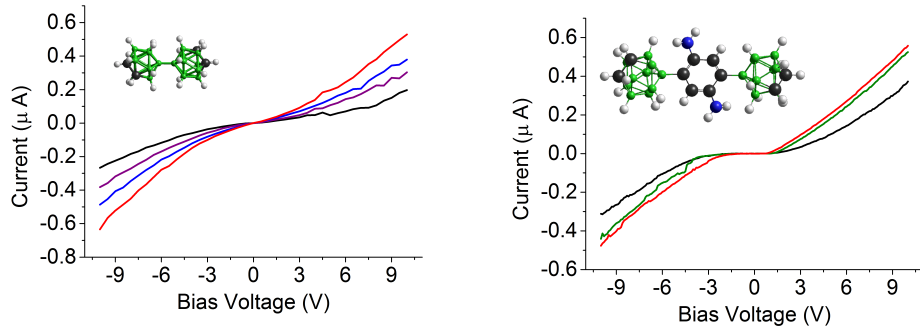


Figure 5.5: I(V) Curves with an external applied magnetic field of zero (black line), 0.1 T (purple line), 0.5 T (blue line), 0.8 T (green line) and 1 T (red line) for thin films of cross-linked ortho-carborane (a) BC and (b) BC:DAB. The insets show the structural model of each film.

As can be seen in these graphs, the negative MR is not only sensitive to the bias voltage, but also to the applied magnetic field, and the constituents added to the boron carbide. For the case of BC films, the relative MR is enhanced from 50% (at negative applied voltage) to 250% (at positive applied voltage), as compared to 50% to 110% for the BC:DAB samples.

The I(V) curves for the BC:DAB film (Fig. 5.5b) and the BC film (Fig. 5.5a), without DAB, key is that as the conductivity in these samples increases as the external magnetic field is increased, again indicating a negative magnetoresistive effect in both types of boron carbide films. At low voltages, in the range of 2 V and +2 V, the current in the BC:DAB films is very low. In contrast, there is no such flat region in the I(V) curve of the BC film (Fig. 5.5a). This difference in the I(V) characteristics of BC:DAB and BC films follows the significant changes in electronic structure at the valence band maximum for the two materials [7,8]. Specifically, valence band photoemission spectra [7,8] indicate that in the BC:DAB material, the states near the valence band maximum are localized on the DAB

moiety, as explained in section 5.2. Therefore, near-threshold promotion of an electron into the conduction band should result in an electron on the icosahedrons moiety, and a hole on the DAB moiety [8].

For a fixed carrier concentration, the conductivity in the samples is proportional to the mean free path of electrons. The negative MR on both samples, suggests a significant spin diffusion length as the carrier concentration in boron carbide is very low. The limited spin diffusion length in the boron carbides studied, may very likely be much longer than the mean free path, and there must be microscopic effects that suppress changes of the spin of the carriers in motion.

The likely mechanism for the large negative MR in these materials involves the polarization of defects along one axis which, in turn, provides enhanced hopping conductivity without spin relaxation, given that the electrodes are magnetic. Such a hopping mechanism explains the flat region of the I(V) curve for BC:DAB (Fig. ??). Formation of an electron (hole) localized on a carborane (DAB) moiety would result in an intrinsic dipole barrier to electron hopping conduction. In contrast, films formed in the absence of diaminobenzene would not exhibit a similar electron-hole separation, and therefore no dipole barrier to electron hopping. As the electrodes are soft magnets, their antiparallel alignment can cause a slight rise in the resistance before the magnetization direction of both electrodes aligns, and then defect polarization then sets in leading to a negative magnetization. This is consistent with MR plotted in Fig. 5.4.

Both samples (BC, and BC:DAB) exhibit significant negative magnetoresistive effect at room temperature. Although the values are surprisingly high, the overall MR effects are expected for main group complex semiconductors with a high number of defects [20,21].

The high MR values, and their manifestation at room temperature suggest practical device applications, especially as such effects are manifested in nanoscale films with facile fabrication.

Also the smaller magneto-resistance in the boron carbide with the aromatic, is consistent with the far longer carrier lifetimes in boron carbide with aromatic additive that without. Fewer defects to polarize may mean that there are also far fewer trapping defects.

References

- [1] Hishiyama Y, Matustani T, Suzuki M, Kaburagi Y, Sugihara K. Journal of Materials Research 2002;17:75.
- [2] Kaburagi Y, Hishiyama Y. In: Proceedings of the Carbon Conference Archive, American Carbon Society; 1997 p. 468.
- [3] Lee S, Mazurowski J, Ramseyer G, Dowben PA. Journal of Applied Physics 1992;72:4925.
- [4] Paquette MM, Li W, Sky Driver M, Karki S, Caruso AN, Oyler NA. Journal of Physics: Condensed Matter 2011;23:435002.
- [5] Pallier C, Leyssale J-M, Truflandier LA, Bui AT, Weisbecker P, Gervais C, et al. Chemistry of Materials 2013. <http://dx.doi.org/10.1021/cm400847t>.
- [6] Behera S, Wilks J, Dowben P, Caruso A, Driver M, Kelber J. Surface Science 2010;604:L51.
- [7] Pasquale FL, Liu J, Dowben PA, Kelber JA. Materials Chemistry and Physics 2012;133:901.
- [8] Pasquale FL, James R, Welch R, Echeverria E, Dowben PA, Kelber JA. ECS Transactions 2013;53:303.

- [9] Pasquale FL, Kelber JA. Applied Surface Science 2012;258:2639-42.
- [10] Jimenez I, Sutherland DGJ, van Buren T, Carlisle JA, Terminello LJ, Himpel F. Journal of Physical Review B 1998;57:13167.
- [11] Jacobsohn LG, Schulze RK, Maia da Costa MEH, Nastasi M. Surface Science 2004;572:418.
- [12] Bao R, Chrisey DB. Thin Solid Films 2010;519:164.
- [13] Bernard L, Caruso AN, Xu B, Doudin B, Dowben PA, PA. Thin Solid Films 2003;428:253.
- [14] Jacobsohn, L.G., Schulze, R.K., Maia da Costa, M.E.H., Nastasi, M. X-ray photo-electron spectroscopy investigation of boron carbide films deposited by sputtering. Surface Science **572** (2004) 418-424
- [15] Losito, I., De Giglio, E., Cioffi, N. and Malitesta, C. Spectroscopic investigation on polymer films obtained by oxidation of *ortho*-phenylenediamine on platinum electrodes at different pHs. J. Mater. Chem. **11** (2001) 1812-1817
- [16] Mthethwa, T., Antunes, E. and Nyokong, T. Photophysical properties of a new water soluble tetra thiamine substituted zinc phthalocyanine conjugated to gold nanorods of different aspect ratios. Dalton Trans., **43** (2014) 8230
- [17] Schoonus, J.J. H.M., Bloom, F.L., Wagemans, W., Swagten, H.J.M. and Koopmans, B. Extremely Large Magnetoresistance in Boron-Doped Silicon. Phys. Rev. Lett. **100** (2008) 127202
- [18] <http://www.hpl.hp.com/techreports/95/HPL-95-60.pdf>
- [19] F.L. Pasquale, Y. Lin, J. Du, J.A. Kelber, J. Phys.: Cond. Matter, 25 105801(2013)

- [20] Mucciolo ER, Lewenkopf CH. Journal of Physics: Condensed Matter 2010;22:273201.
- [21] Fritz L, Vojta M. Reports on Progress in Physics 2013;76:032501.

Chapter 6

CONCLUSIONS

Metal/semiconductor interface formation was studied by X-ray photoemission spectroscopy. It was found that boron carbide-based semiconductors behave different from other semiconductor materials, since it presents Schottky barrier formation when working with p-type heterojunctions. Being the work function of the gold, the metal used for this study, bigger than this for the semiconductor, it is expected to see signatures of ohmic contacts in the interface between the metal and the semiconductor, i.e., binding energies shifting to small values, or not change in the binding energy. However, shifting of the binding energies for the B(1s) and C(1s) core levels to high energies was found, can be explained by having a Schottky barrier formation in the interface. The opposite situation is found when working with n-type boron carbide semiconductors and gold. No band bending signatures were found, therefore an ohmic contact is assigned to this surface interaction, confirming the unusual behavior of these heterojunctions. Inclusion of the aromatic compounds aniline seems to increase the Schottky barrier formed on the interface in the case of p-type heterojunctions.

From electrical and optical measurements on these boron carbide-based heterojunctions, it was found that semiconducting boron carbides exhibit significantly enhanced

electron-hole separation with inclusion of the aromatic compounds. For the case of *ortho*-carborane boron carbide films, carrier lifetimes increase from $35 \mu s$, for the pure boron carbide, to $350 \mu s$ with pyridine inclusion, and even better to $2.5 ms$ with benzene inclusion. The findings of substantially enhanced electron-hole separation and carrier lifetime in the doped films versus pure boron carbide films are certainly encouraging for the application of these materials as solid state neutron detectors.

In the case of the addition of pyridine linking groups to PECVD semiconducting hydrogenated boron carbide films, synthesized on n-type silicon, it was found that charge collection increases, after neutron capture, in a heterojunction diode with silicon at zero bias, and the charge collection is much improved compared to heterojunction diodes fabricated by PECVD but without pyridine. The spatial overlap of the HOMO and LUMO states in cluster calculations, if applicable to the solid, suggests that exciton decay is facile, but hindered by symmetry constraints.

Finally, it was shown that semiconducting boron carbide polymers, formed by site-specific cross-linking of orthocarborane icosahedra with and without 1,4 diaminobenzene, exhibit significant negative magnetoresistive effect at room temperature. Values over 450% negative magnetoresistance, depending on the bias voltage, are found for the pure boron carbide, while for samples with diaminobenzene doping it was about 100%. Although inclusion of diaminobenzene does not improve the negative magnetoresistance values, other aromatic compounds need to be tested to determine whatever or not doping will affect the magnetoresistance of the films.

Chapter 7

FUTURE DIRECTIONS

The results of this work have showed that better boron carbide based semiconductors can be achieved. However, more testing on neutron detection is needed to fully characterized these semiconductors. In part, an effort towards this end: a passive lightweight neutron detector, UN-DANSON¹, has been designed and placed on the International Space Station (ISS).

The detector contains two different types of materials commonly used for neutron detection, high quality lithium tetraborate crystals with different isotopic compositions, and the boron carbide-based heterojunctions investigated in this dissertation. Both types of detectors are covered by various thicknesses of MakrolonTM polycarbonate material. Figure 7.1 shows a picture of the entire package.

The MakrolonTM polycarbonate is used to slow down the highly energetic incident neutrons, and samples are placed in different positions inside the box, such that each sample will be behind various thicknesses of the moderator material, therefore, irradiation from different energetic neutrons can be studied.

¹ University of Nebraska Detector for the ANalysis of SOLar Neutrons.

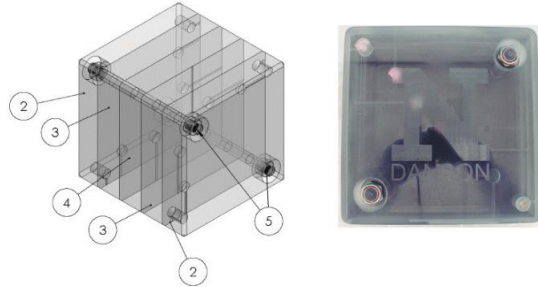


Figure 7.1: Left: Schematic of the MakrolonTM plate assembly. The end plates (2), side plates (3), center plate (4) and locking bolts (5) are indicated. Right: The assembled solar neutron detector.

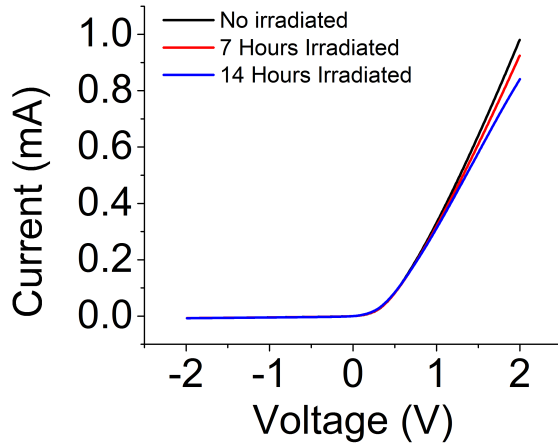


Figure 7.2: I(V) curve for boron carbide with pyridine before (black line), after 28 hours (red line), and after 84 hours (blue line) of neutron irradiation.

In the case of the boron carbide-based heterojunctions, all samples were previously characterized by electrical measurements, I(V) and C(V) curves. Hence, by looking at changes in the transport measurements it will be possible to determine how neutron irradiation affects the electrical properties of the detectors. Since previous data (see Fig. 7.2) have shown that several hours of neutron irradiation can modify the I(V) curves, it is expected to see significant changes in the electrical response after being irradiated for several months.

On other hand, this dissertation showed that Au/boron carbide-based semiconductors present an unusual behavior when gold (Au) is deposited on the surface. To help in the understand-

ing of these findings, different metals need to be tested, specially metals with lower work function compared to that of the boron carbide, so the four cases discussed in section 3.2 will be covered.

It was shown as well, that concentration of the aromatic compounds affects the band gap of the semiconductors, thus, not only variations on the metal can be interesting to study, but also how the aromatic compound to boron carbide ratios can increase/decrease the Schottky barrier formed at the interface.